Published in final edited form as:

*Annu Rev Biomed Eng*. 2020 June 04; 22: 309–341. doi:10.1146/annurev-bioeng-062117-121105.

# Integrated Biophysical Modeling and Image Analysis: Application to Neuro-Oncology

**Andreas Mang**[1,*], **Spyridon Bakas**[2,*], **Shashank Subramanian**[3], **Christos Davatzikos**[2], **George Biros**[3]

[1]Department of Mathematics, University of Houston, Houston, Texas 77204, USA;

[2]Center for Biomedical Image Computing and Analytics (CBICA); Department of Radiology; and Department of Pathology and Laboratory Medicine, Perelman School of Medicine, University of Pennsylvania, Philadelphia, Pennsylvania 19104, USA;

[3]Oden Institute of Computational Engineering and Sciences, The University of Texas at Austin, Austin, Texas 78712, USA;

## Abstract

Central nervous system (CNS) tumors come with vastly heterogeneous histologic, molecular, and radiographic landscapes, rendering their precise characterization challenging. The rapidly growing fields of biophysical modeling and radiomics have shown promise in better characterizing the molecular, spatial, and temporal heterogeneity of tumors. Integrative analysis of CNS tumors, including clinically acquired multi-parametric magnetic resonance imaging (mpMRI) and the inverse problem of calibrating biophysical models to mpMRI data, assists in identifying macroscopic quantifiable tumor patterns of invasion and proliferation, potentially leading to improved (*a*) detection/segmentation of tumor subregions and (*b*) computer-aided diagnostic/prognostic/predictive modeling. This article presents a summary of (*a*) biophysical growth modeling and simulation, (*b*) inverse problems for model calibration, (*c*) these models' integration with imaging workflows, and (*d*) their application to clinically relevant studies. We anticipate that such quantitative integrative analysis may even be beneficial in a future revision of the World Health Organization (WHO) classification for CNS tumors, ultimately improving patient survival prospects.

### Keywords

glioblastoma; tumor growth; biophysical modeling; image analysis; radiomics; multi-parametric imaging; model calibration

andreas@math.uh.edu.

*These authors contributed equally to this article

DISCLOSURE STATEMENT

The authors are not aware of any affiliations, memberships, funding, or financial holdings that might be perceived as affecting the objectivity of this review.

Errata

An online log of corrections to *Annual Review of Biomedical Engineering* articles may be found at http://www.annualreviews.org/errata/bioeng

## 1. INTRODUCTION

Gliomas are the most common primary central nervous system (CNS) malignancies. Therapeutic intervention for their most aggressive manifestation—glioblastoma multiforme (GBM) (1, 2)—remains palliative. Gliomas exhibit highly variable clinical prognoses, and they usually contain various heterogeneous subregions with variable histologic and genomic phenotypes. This intrinsic heterogeneity is also characteristic of their radiographic phenotypes—subregions appear with different intensity profiles across multi-parametric magnetic resonance imaging (mpMRI) scans, reflecting differences in tumor biology and pathophysiology (see Figure 1 for an example). Our discussion is limited to clinical in vivo studies in humans; we do not address work in animal models, nor ex vivo or in vitro studies.

Personalized precision medicine aims at developing fine-tuned, patient-specific treatment strategies. In the context of neuro-oncology, these include surgery, radiotherapy, and chemotherapy planning. Fine-tuning complex clinical treatments necessitates an accurate diagnosis. The fundamental premise that underlies the work of several groups is that biophysical simulations in combination with sophisticated computational methods targeting radiographic features—so-called radiomics—can augment existing clinical tools, and consequently aid clinical decision making and patient management.

Current clinical practice is based on the analysis of radiographic imaging data and biopsy, i.e., the ex vivo analysis of tissue. Brain tumors have been classified according to the World Health Organization (WHO) morphologic-histopathologic classification (5), from grade I to IV with increasing aggressiveness. In 2016, the WHO revised its classification scheme into an integrated morphologic-histopathologic and molecular-cytogenetic characterization for CNS tumors (6) in an attempt to improve tumor stratification, potentially leading to an improved patient prognosis. However, even with the addition of molecular-cytogenetic data, CNS tumors—and particularly gliomas—remain challenging to characterize, primarily since their classification is still based on ex vivo postoperative tissue analysis (i.e., biopsies; see the sidebar titled Shortcomings of Biopsies).

In contrast to tissue analysis, imaging can noninvasively capture in vivo the spatial heterogeneity within the whole extent of the tumor (even in deep-seated/inoperable tumors), thereby minimizing potential bias due to only sampling a limited portion of the tumor; moreover, it can be performed repeatedly. Since glioma patients routinely undergo multiple mpMRI scans—before surgery and during adjuvant treatment—there are ample data available that could help to evaluate the status of the tumor and the surrounding tissue, provide quantitative features for patient assessment, and potentially positively influence personalized treatment and prognosis.

Despite considerable advances in medical imaging sciences, significant challenges remain. Clinicians face substantial dilemmas during neuroimaging evaluation of patients. For example, for preresection patients, a precise quantification of the infiltration of tumor cells into surrounding healthy tissue beyond the visible abnormalities in imaging remains challenging. Differentiation between tumor progression and radiation/treatment effects (a clinical problem termed pseudo-progression) can be difficult based on current imaging

criteria (7); failure to recognize pseudoprogression can lead to premature termination of an effective chemotherapy. On top of that, there exist sensitivities with respect to scanner-specific settings and parameters.

In recent years, there has been mounting evidence that quantitative mpMRI analysis can characterize CNS tumors comprehensively and provide critical information about various biological processes within the tumor microenvironment as well as associations with underlying cancer molecular characteristics (8–27). Community efforts have created high-quality datasets that can be used to better understand cancer (28–36). Advances in computational inference and machine learning (including deep learning) have dramatically improved our ability to process large datasets. All these advances have facilitated the development of computational methods for high-throughput extraction of quantitative features using sophisticated algorithms. These algorithms are used for image segmentation and can produce quantitative metrics from imaging data, which in turn can be used to produce critical information for patient characterization, especially when fused with other clinical data.

Although purely image-based correlation analysis (31) is very successful, there are still many challenges related to robustness (sensitivity to local minima and dataset overfitting) and extrapolation, since most medical datasets are limited compared to the complexity of the underlying processes. Many research studies have sought to extract information using biophysical mode priors in the brain (4, 37–44), as well as other organs, such as breast, kidney, pancreas, liver, prostate, and lungs (45–56). Developments in computational modeling of untreated gliomas, as well as models of polyclonal gliomas following chemotherapy and surgical resection, can help capture important information for diagnostic, planning, and prognostic purposes (57–70). The key benefits of these approaches are that they rigorously follow mathematical and physical principles and are also quantitative and reproducible. They can, in combination with machine learning approaches, help consolidate complex imaging data (see Figure 1 for an illustration). They can unveil hidden spatiotemporal variables (i.e., clinical markers that are not directly observable from clinical data). Consequently, the integration of computational models with imaging offers great promise of providing a more complete understanding of clinically relevant entities, thereby improving precision diagnostics and therapeutics. These advances would in turn further improve the clinical outcome and may, ultimately, become an integral part of a new form of WHO classification of CNS tumors. However, the development of clinically reliable tumor growth models and their integration with imaging data, which at its core is an inverse problem (71), remains a significant challenge for various reasons (see the sidebar titled Challenges for Integration of Mathematical Models with Imaging).

The significance of the integration of computational models of tumor growth with imaging is threefold: automatic segmentation of patient images using normal subject images to create spatial (shape) priors; mapping of functional information from atlases to patients (critical in neuro-surgery); and parameter calibration of biophysical models. Prior work has shown that biophysical models offer complementary information that relates to tumor aggressiveness and clinical outcome. We summarize some relevant work and its clinical applications in Table 1.

In this article, we (*a*) review state-of-the-art approaches in tissue-level brain tumor modeling, (*b*) present mathematical strategies for model calibration, (*c*) discuss the integration of biophysics simulations with medical imaging data to aid imaging workflows and, ultimately, generate predictive capabilities, and (*d*) showcase different clinical studies that benefit from such an integration. We focus on forward simulation of tumor growth on a macroscopic scale (tissue level) and inverse problem formulations that connect sophisticated forward models with imaging methods (see Figure 1). We review and present formulations and methodology for the simulation of tumor growth in Section 2. We describe approaches for model calibration and biophysics inversion in Section 3. We discuss the integration of biophysics simulation and computational methods for radiomics in Section 4. We provide results from clinically relevant studies in Section 5.

## 2. TUMOR GROWTH MODELING AND SIMULATION

There is a long tradition in the design of mathematical models of tumor progression (100–103). Recent advances in mathematics and computational engineering have led to a rich pool of computational models with unprecedented complexity. These models present us with significant challenges; they encompass multiscale, strongly heterogeneous, and coupled multiphysics behavior. Models range from simple population growth models (72) to complex multiphysics, multispecies, space-time models (78, 104, 105), with dynamical systems that describe tumor progression on various scales of observation, including molecular (106), cellular (107, 108), tissue (109–111), and multiscale representations (112–114). We limit ourselves to models that can be integrated with in vivo morphological or functional medical imaging, such as magnetic resonance imaging (MRI), computed tomography (CT), and positron emission tomography (PET)—models that yield outputs on a tissue scale. Cancer progression is typically formulated as a dynamical system [a set of ordinary differential equations or partial differential equations (PDEs)] based on principles of conservation and constitutive laws. For tissue-level models, tumor cells are not tracked individually but modeled as a concentration or volume fraction (assuming constant density) $c(\boldsymbol{x}, t)$, where $\boldsymbol{x} \in \Omega \subset \mathbb{R}^3$ and $t \in [0, 1]$ (where $t$ has been nondimensionalized to the unit interval). Depending on the model, $c$ can be a scalar (single species) or a vector (multiple species).

The seminal works (109–111) are based on the assumption that cancerous cells originate from either cell division (proliferation) or cell migration. These principles can be captured by reaction-diffusion (RD) equations of the form

$$\partial_t c - \kappa \mathscr{D} c - f(c) = 0 \text{ in } \Omega \times (0, 1], \; c = c_0 \text{ in } \Omega \times \{0\}, \tag{1.}$$

with zero flux boundary conditions on $\partial\Omega$ and initial condition $c_0$ at $t = 0$. $\mathscr{D}$ is a diffusion operator that models the migration of cancerous cells into surrounding healthy tissue, parameterized by the diffusion coefficient $\kappa \geq 0$. The functional $f$ models the proliferation of tumor cells parameterized by $\rho \geq 0$; the most common model is a logistic growth function $f(c) = \rho c(1 - c)$. Further, $\mathscr{D}c := \nabla \cdot \boldsymbol{K} \nabla c$ with gradient $\nabla := (\partial_1, \ldots, \partial_d)$, divergence operator $\nabla \cdot : = \sum_{i=1}^{d} \partial_i$ and $\boldsymbol{K} : \overline{\Omega} \to \mathbb{R}^{d \times d}$. The tensor field $\boldsymbol{K}$ controls the diffusion within

different tissue compartments. Initial models (109–111) considered distinct diffusion rates in white matter (WM) and gray matter (GM). These models were extended to account for a preferential (anisotropic) diffusion within WM by integrating diffusion tensor imaging data (37, 40, 115–119).

While the single-species model (Equation 1) can phenomenologically capture the overall dynamics of tumor growth, it does not capture the imaging phenotype of gliomas. For example, GBM typically presents with an enhancing rim surrounding a necrotic core, with significant peritumoral edematous/tumor-infiltrated tissue (ED) (see Figure 1 for an example). Also, the model in Equation 1 does not capture the mechanical deformation of the brain parenchyma, the so-called mass effect (37, 45, 47, 75, 77, 90, 98, 120–122). Models that attempt to capture the heterogeneous phenotype use multiple species of tumor cells with different underlying hypotheses that govern their evolution (see Figure 2). One class of models assumes that tumor cells exist in interchangeable states based on the nutritional condition of their environment. A popular hypothesis is “grow or go,” which stipulates that invading tumor cells are minimally proliferative and vice versa (123). Models that follow this hypothesis represent tumor progression as (a cycle of ) two phases: an initially exclusively proliferative phase followed by an invasion of tumor cells into surrounding tissues. This second phase can then possibly transition back to a proliferating phenotype, which encourages recurrence and growth of metastatic tumors. Other models (124) consider these phases to be difficult to isolate; they are modeled to occur simultaneously. As an example, consider a multispecies model that accounts for mass effect and in which $\boldsymbol{c}(\boldsymbol{x}, t) := (c_{\mathrm{P}}(\boldsymbol{x}, t), c_{\mathrm{I}}(\boldsymbol{x}, t), c_{\mathrm{N}}(\boldsymbol{x}, t))$ consists of proliferating (P), invading (I), and necrotic (N) tumor cell phenotypes, respectively.

The associated system of PDEs (including mass effect) is given by (122, 125)

$$\partial_t \boldsymbol{c} + \nabla \cdot (\boldsymbol{c} \otimes \boldsymbol{v}) - \kappa \mathscr{D} \boldsymbol{c} - \boldsymbol{f}(\boldsymbol{c}) - \boldsymbol{g}(\boldsymbol{c}, \boldsymbol{n}) = 0 \, \Omega \times [0, 1] \tag{2a.}$$

$$\partial_t \boldsymbol{n} - \mathscr{D} \boldsymbol{n} - \boldsymbol{h}(\boldsymbol{c}, \boldsymbol{n}, \boldsymbol{m}) = 0 \, \Omega \times [0, 1] \tag{2b.}$$

$$\nabla \cdot (\lambda \nabla \boldsymbol{u} + \mu (\nabla \boldsymbol{u} + \nabla \boldsymbol{u}^{\mathrm{T}})) = \boldsymbol{b}(\boldsymbol{c}) \, \Omega \times [0, 1] \tag{2c.}$$

$$\partial_t \boldsymbol{u} = \boldsymbol{v} \, \Omega \times [0, 1] \tag{2d.}$$

$$\partial_t \boldsymbol{m} + \nabla \cdot (\boldsymbol{m} \otimes \boldsymbol{v}) = \boldsymbol{s}(\boldsymbol{m}, \boldsymbol{c}) \, \Omega \times [0, 1], \tag{2e.}$$

with initial conditions $c = c_0$ and $\boldsymbol{m} = \boldsymbol{m}_0$; $\otimes$ denotes the outer product, $\boldsymbol{u}(\boldsymbol{x}, t)$ is the displacement field, and $\boldsymbol{v}(\boldsymbol{x}, t)$ is the derived velocity field.

First, notice the two-way coupling between mass effect and tumor growth due to an advective term in the RD equation and a forcing term in the linear elasticity term. Second, the mass effect is modeled using a simple linear elasticity model with a forcing proportional to the gradient of $c$. More complex models that account for large deformations, growth

stresses, residual stress, and tissue microstructure exist (126–128). The linear elasticity model is parameterized by the inhomogeneous Lamé coefficients $\lambda: \overline{\Omega} \to \mathbb{R}$ and $\mu: \overline{\Omega} \to \mathbb{R}$; they depend on the underlying tissue type. The function $\boldsymbol{b} \propto \nabla c$ represents a body force acting on the brain parenchyma (37, 86, 98, 122). Finally, Equations 2d and 2e model the evolution of healthy tissue volume fractions $\boldsymbol{m}(\boldsymbol{x}, t) := (m_W(\boldsymbol{x}, t), m_G(\boldsymbol{x}, t), m_F(\boldsymbol{x}, t))$, where W, G, and F designate WM, GM, and cerebrospinal fluid (CSF), and initial condition $\boldsymbol{m}_0(\boldsymbol{x}) := (m_{W,0}(\boldsymbol{x}), m_{G,0}(\boldsymbol{x}), m_{F,0}(\boldsymbol{x}))$. The field $\boldsymbol{s}(\boldsymbol{m}, c)$ models the rate of change of tissue due to sources and sinks. For example, it can account for CSF leakage and/or loss of healthy GM and/or WM cells due to tumor progression. We illustrate qualitative simulation results for this model in Figure 2. In addition to the spatiotemporal dynamics of tumor cells, we also account for nutrient supply and tumor-induced ED. These quantities are represented as a vector-valued function $\boldsymbol{n}(\boldsymbol{x}, t) := (n_O(\boldsymbol{x}, t), n_E(\boldsymbol{x}, t))$ consisting of two concentration maps for nutrients/oxygen (O) and ED (E), respectively. Changes in $\boldsymbol{n}$ are modeled via a diffusion operator $D$ and a source and/or sink term $\boldsymbol{h}(\boldsymbol{c}, \boldsymbol{n}, \boldsymbol{m})$. The sources and sinks can, for example, account for the supply and consumption of oxygen and the leakage of ED into the extracellular matrix due to migrating tumor cells. The RD equation for the tumor phenotype $\boldsymbol{c}$ includes a sink and/or source term $\boldsymbol{g}(\boldsymbol{c}, \boldsymbol{n})$. The precise form of $\boldsymbol{g}$ depends on the underlying hypotheses of the growth model. The grow-or-go hypothesis, for example, stipulates mutually incompatible proliferating and migrating phenotypes through different reaction and diffusion operators. The transition between phenotypes depends on the local oxygen concentration. The mass effect is modeled using a linear elasticity equation. We illustrate qualitative simulation results for this model in Figure 2.

Despite their phenomenological character, these types of models (in particular the single-species model coupled with mass effect) can successfully capture the overall appearance of tumors in mpMRI (37, 40, 74, 79, 115, 118, 129). They have been used to (*a*) study tumor growth patterns in individual patients (37, 79, 109, 115, 118), (*b*) extrapolate the physiological boundary of tumors (40, 81), and (*c*) study the effects of clinical intervention (41, 51, 83, 85, 89, 90, 130). Applications for these types of models beyond brain tumor imaging include breast (90) and pancreatic cancer (129) imaging. Continuum models of the form of Equation 1 have also been extended to account for the evolution of cancer progression on the cellular scale (e.g., accounting for healthy, proliferative, quiescent, and necrotic cellular phenotypes), the subcellular scale, and the molecular scale (for example, accounting for signaling pathways) (78).

## 3. INVERSE PROBLEMS FOR PARAMETER CALIBRATION

Next, we discuss the inverse problem of estimating biophysical model parameters, $\boldsymbol{p}$, for a given tumor growth model, $F$, with the ultimate goal to provide a framework for patient-specific tumor growth simulations and model predictions. A natural approach to estimate $\boldsymbol{p}$ is to formulate a PDE-constrained optimization problem.

### Remark 1.

We discuss only the problem of estimating tumor-specific parameters. The integration of tumor modeling with mpMRI is described in Section 4. In practice, imaging is used to derive

information for calibrating the model. For example, $c_{\text{OBS}}$, which we define in the next paragraph, is implicitly derived from mpMRI data.

**3.1. Deterministic Formulations—**The input to our problem is a series of observations of tumor cell densities $c_{\text{OBS}}$ (partially observed tumor data) at specified time instances $\{t^j\}_{j=1,\ldots,n_t}$ within a given time interval $[0,\ T]$ with final time $T > 0$. In the inverse problem, we seek parameters $\boldsymbol{p}$ such that the model output $c(\boldsymbol{x},\ t)$ (i.e., the simulated cell density or tumor cell probability maps) matches these observations. In a general format, we can represent this calibration of tumor models as a PDE-constrained optimization problem of the form

$$\underset{p}{\text{minimize}} \frac{1}{2}\sum_{j=1}^{n_t}\int_0^T\int_\Omega \delta(t-t^j)\left(c(\boldsymbol{x},t)-c^j_{\text{OBS}}(\boldsymbol{x})\right)^2 dx\,dt + \mathscr{R}(\boldsymbol{p}) \text{ subject to } \mathscr{F}(\boldsymbol{p},c) = 0. \quad (3.)$$

This formulation balances the data fidelity with regularity assumptions on the model parameters $\boldsymbol{p}$ (the inversion variable of our problem). We consider a squared $L^2$ distance to measure the discrepancy between $c^j_{\text{OBS}}(x)$ and the model output $c(\boldsymbol{x},\ t)$. The operator $\mathscr{F}$ is the forward tumor model (see Section 2 for examples). The inversion variable $\boldsymbol{p}$ (e.g., the growth rate $\rho \geq 0$) and the state variable $c$ (e.g., the density of tumor cells) are the unknowns of our problem. $\delta$ is a Dirac delta function to pick the time points $t^j$ in $[0,\ T]$ to which the data $c^j_{\text{OBS}}$ are associated. The functional $\mathscr{R}$ in Equation 3 is introduced to alleviate the ill-posedness of the inverse problem of recovering $\boldsymbol{p}$ from $c_{\text{OBS}}$. The basic idea is to stably compute a locally unique solution to a nearby problem by imposing prior knowledge based on an adequate regularization scheme (in our case, represented by $\mathscr{R}$).

**Remark 2.:** In Equation 3, we assume that we are given a time series $c^j_{\text{OBS}}$, $j = 1, \ldots, n_t$. In a typical clinical setting, we are usually given a single snapshot for $c_{\text{OBS}}$. Indeed, when a patient presents with symptoms, the tumor is usually large, and treatment (surgery, chemotherapy, or radiation) starts immediately. Consequently, it is not practical to assume a time series of data; any treatment that takes place needs to be incorporated into the models, which poses additional difficulties. This is not the case in animal studies (which we do not consider here). We discuss strategies to resolve this issue of limited data in Section 4.

The standard approach for solving Equation 3 is to introduce an additional unknown—the Lagrange multiplier $\lambda$—and derive the stationarity conditions for the Lagrangian $\mathscr{L}(c, \boldsymbol{p}, \lambda) := \mathscr{J}(\boldsymbol{p}) + \langle \mathscr{F}(c, \boldsymbol{p}), \lambda \rangle_{L^2(\Omega)}$ ($\mathscr{J}$ denotes the objective functional in Equation 3). Derivative-free optimization (45–47, 51, 98, 115, 118, 119, 121, 131), automatic differentiation, and finite-difference approximation of the gradient (74) are other options. Derivative-free strategies are easy to implement (they only require routines to evaluate $\mathscr{F}$ and $\mathscr{J}$ for trial parameters $\boldsymbol{p}$). However, they lead to suboptimal algorithms with slow convergence, typically resulting in an excessive number of iterations and high computational costs (perhaps run times of days on medium-size clusters). This renders these methods

impractical, especially for problems parameterized by a large number of unknowns $\boldsymbol{p}$. References 98, 116, 129, and 131–135 use adjoint information, i.e., methods that exploit analytical derivatives. These methods are preferable to derivative-free approaches as they offer better convergence guarantees, are founded on rigorous mathematical principles, can reveal structure (sensitivities) that can be rigorously analyzed, and can be exploited for further integration with imaging (e.g., construction of priors for Bayesian inference).

Various approaches and formulations have been considered. In Reference 134, the tumor is modeled as a radially symmetric spheroid. More complex tumor models are described elsewhere (77, 98, 129). Hogea et al. (98) derive adjoint equations in one dimension; derivative-free optimization is used for three dimensions (3D). Liu et al. (129) extend this work, providing results for an adjoint-based method for 3D problems. Wong et al. (77) follow up on References 98 and 129; the key difference is that they use a hyperelastic mass-effect model as opposed to linear elasticity. Complex multispecies models are considered in References 132 and 135. Other works describe an inversion framework to determine the initial distribution of tumor concentration of a nonlinear RD PDE using adjoint-based methods (91, 116, 136).

All works discussed above calibrate only for a subset of unknown parameters $\boldsymbol{p}$. For example, Scheufele et al. (91) assume a known reaction coefficient $\rho$ and invert for the tumor initial condition $c_0(\boldsymbol{x})$ and a scalar diffusion coefficient $\kappa > 0$. Indeed, it is not possible to reliably invert for all parameters—even for simple RD PDEs—due to the ill-posedness of the inverse problem (119, 137). Additional modeling assumptions can alleviate some of these issues. Rekik et al. (79) estimate a localized initial condition along with the tumor diffusion coefficient for a traveling wave approximation. This localization enables the estimation of more biophysically meaningful diffusion rates. Jaroudi et al. (138) attempt to reconstruct sparse tumor initial conditions while fixing the other parameters of a 3D nonlinear RD model. Subramanian et al. (137) describe a framework to estimate all unknown parameters of a 3D nonlinear RD growth model, i.e., the reaction coefficient, the diffusion coefficient, and the tumor initial distribution. Sparsity constraints on the tumor initial condition and constraints on its maximum norm are introduced. This work extends that of Reference 91 with a greedy pursuit algorithm for imposing sparsity constraints.

**3.2. Probabilistic Formulations—**While the deterministic approach described above is adequate for identifying optimal parameters $\boldsymbol{p}^\star$ such that model predictions match some observed data $c_{\text{OBS}}$, its practical value remains limited. Indeed, solving Equation 3 only provides us with point estimates $\boldsymbol{p}^\star$. In practice, we are interested in predicting some future quantity of interest $q(\boldsymbol{p})$, say, the probability of tumor recurrence after surgery. Due to uncertainties in the data $c_{\text{OBS}}$, the inversion variable $\boldsymbol{p}$, and the mathematical model $\mathcal{F}$, as well as the nonconvexity of the inverse problem, we require confidence intervals for $q(\boldsymbol{p})$ and not just point estimates $\boldsymbol{p}^\star$. These can be achieved through a probabilistic formulation of the inverse problem, the result of which is a probability density function that characterizes our confidence in $q(\boldsymbol{p})$. The appropriate framework for dealing with such problems is Bayesian inference (71).

Bayesian inference yields a systematic framework that rigorously follows mathematical and physical principles and enables us to address key questions underlying predictive computational modeling. We can quantify uncertainties as they propagate through all steps of our system, and we can assess model validity and adequacy. While these features are appealing, a serious drawback is the significant increase in computational burden. Approaches that consider a probabilistic framework are described elsewhere (73, 76, 83, 88, 130, 139–142). Some are based on RD-type systems (130, 140, 143). Others present methodology for statistical model calibration and, in addition, provide methodology and results for model selection and validation (76, 88, 139, 141). They, like Reference 144, consider phase-field models. Reference 88 describes an extension of the work of Oden and colleagues (76, 139, 141), considering a set of eight RD-type models and five variants of phase-field models of varying complexity. References 73, 142, and 145 are restricted to simplistic models of spheroid tumor growth. The focus is on developing effective stochastic computational methods. The works mentioned so far focus mostly on algorithmic developments. Kahle et al. (146) discuss theoretical considerations instead, in an extension of Reference 144 to the probabilistic setting. They, like Oden and colleagues (76, 139, 141), consider a phase-field model. Well-posedness results of the posterior measure for general prior measures are provided.

We note that several modeling and computational challenges in this area remain open (see the sidebar titled Challenges and Open Questions in Biophysical Inversion).

## 4. INTEGRATION WITH MAGNETIC RESONANCE IMAGING

The integration of biophysical tumor growth models with mpMRI can be considered as a two-way coupled problem, where imaging provides the data required to drive the calibration of a biophysical model through the solution of an inverse problem, and biophysical models can define priors for image analysis and introduce additional biomarkers. Imaging data for calibration include the geometry of the brain and the implicit characterization of the underlying tissue, via intensity information from mpMRI modalities. Biophysical models provide probabilistic information about tumor infiltration in specific tissues to, e.g., enable or guide common imaging workflows, such as image segmentation (4, 25, 91, 96, 147) or image registration (92, 98, 148, 149). Biophysical model parameters can also play the role of biomarkers, for example, the reaction and diffusion coefficients, and parameters of the initial condition such as focality and location.

### 4.1. Imaging Workflows: Image Segmentation and Registration

In image segmentation, we seek a classification of the medical imaging data into different subregions, each of which corresponds to tissue with distinct pathophysiological properties. In our application, we are interested in differentiating healthy and diseased brain tissue and possibly subdividing further the healthy and nonhealthy regions. In neuro-oncology for high-grade gliomas, one typically differentiates the anatomical brain regions of WM, GM, and CSF from the abnormalities visible in the vicinity of the primary tumor site—the peritumoral ED and the tumor core (TU) region, which can be further differentiated into the enhancing tumor (ET) region and the union of the necrotic and nonenhancing parts (NE). An

accurate segmentation of tumor subregions is relevant for diagnosis and treatment planning. However, tumor segmentation is quite challenging because the tumor regions are defined through intensity changes relative to the surrounding normal tissue, as well as varying intensity distributions disseminated across multiple modalities, that are often subtle. Additional factors are imaging artifacts such as noise, motion, or magnetic field inhomogeneities. The manual annotation of region boundaries is time consuming and prone to misinterpretation, human error, and observer bias (150, 151). To remove these biases, it is desirable to design automatic approaches. To date, the best results are achieved by machine learning techniques (31, 152). These methods can be augmented with biophysical simulations (94, 95). For example, one can use simulations as a data augmentation strategy for training neural networks (153).

In image registration, we are interested in computing a spatial transformation $\boldsymbol{y}$ that maps points in one image to corresponding points in another image. Image registration has evolved into an indispensable tool in medical image analysis (154). In the context of monitoring disease progression or treatment response, images of a brain tumor will be acquired at different points in time with changes in morphological appearance, texture, structure, shape, and field of view (95, 155). These changes make an accurate registration a delicate matter. While changes in pose can be compensated for in a stable way (155), it is challenging to compensate for nonlinear deformations $\boldsymbol{y}$ (156). Especially challenging is registration between pre- and postresection imaging scans (149, 157), where parts of the tumor are missing due to resection. Aside from monitoring a single patient, we might be interested in gathering statistical information across a population of patients (16, 158). This necessitates the registration of patient individual scans to a common anatomical atlas image, which—even in the absence of a tumor—is challenging due to interpatient anatomical variability. In the presence of a tumor, this registration requires finding correspondences between two topologically different images—one with and one without a tumor. Similarly, we can use image registration to solve the segmentation problem by transferring labels for anatomical regions defined in the atlas space to unseen patient data (4, 91, 92, 159). A simple strategy is to mask the tumor area (known as cost-function masking) (93, 160, 161) or to relax the registration in the area affected by the tumor (162). This yields poor registration quality for tumors with severe mass effect. Another strategy is to simultaneously invert for the deformation map and a drift in intensity representing the imaging abnormality (163). While this may produce acceptable results for the purpose of atlas-based segmentation and registration, it cannot be used for model prediction and tumor characterization (16, 27)—our ultimate goal. One remedy is the integration of image registration with biophysical modeling.

### 4.2. Integration of Biophysical Modeling with Imaging

In aggressive tumors, time series of images of patients who have not undergone treatment are in general unavailable [this is not true of animal studies (74, 88, 133)]. The fact that we do not have access to longitudinal data without treatment makes the integration of biophysical modeling with imaging even more challenging. We need to calibrate complex PDE models (see Section 2) based on a single snapshot in time. Since the model is typically a dynamical system, it is impossible (without regularization) to calibrate model parameters

using a single-time dataset. Moreover, we do not have data for the initial state, i.e., an image of the patient's brain without a tumor, or any other information about time history. A common strategy is to simulate the progression of the tumor in a healthy (tumor-free) image (see Figure 3).

This is suboptimal because anatomical differences introduce significant errors (115, 118). One approach for resolving these anatomical differences is to simultaneously invert for a model-based deformation (spatial transformation) $\boldsymbol{y}$ that maps the atlas to the patient anatomy (or vice versa) (4, 91, 92, 98, 99, 148, 159, 164, 165). The models described by References 92, 148, 159, and 165 are oversimplified (e.g., purely mechanical); they do not allow for recovering growth patterns of tumors with complex shapes, nor do they provide information about progression or infiltration of tumor cells into healthy tissue. We discuss two frameworks developed by our group that do not have these limitations. They integrate complex biophysical simulations with image registration in an attempt to aid imaging workflows and provide predictive capabilities. The first is the Glioma Image Segmentation and Registration (GLISTR) framework (4, 96); the second is the Scalable Integrated Biophysics-based Image Analysis (SIBIA) framework (91, 136, 164, 166). Variants of these frameworks are already used in clinically relevant studies (4, 25, 32, 39, 140, 167) (see Section 5).

#### 4.2.1. Glioma Image Segmentation and Registration (GLISTR and GLISTRboost).—

GLISTR (4) is a generative approach for simultaneously registering a probabilistic atlas of a healthy population to brain tumor mpMRI scans and segmenting the apparent brain in various subregions. The output of GLISTR is a posterior probability map $\boldsymbol{\pi}_i$: $\Omega \rightarrow [0, 1]$, $i \in \Theta$ and a label map $\xi$: $\Omega \rightarrow \Theta$, $\Theta := \{\text{W, G, TU, F, ED}\}$. GLISTR incorporates the glioma growth model described elsewhere (98, 121, 168; see also Section 2). We define the probability maps $\boldsymbol{\pi}_i$ as conditional probabilities $\boldsymbol{\pi}_i(\boldsymbol{x} | \boldsymbol{p})$ on the unknown tumor parameters $\boldsymbol{p}$.

The joint registration and segmentation problem solved in GLISTR is as follows: We are given a vector $\boldsymbol{q}(\boldsymbol{x}) := (q_1(\boldsymbol{x}), \ldots, q_k(\boldsymbol{x})) \in \mathbb{R}^k$ of observations (imaging intensities) that correspond to $k$ MRI modalities (input to our problem; see Figure 3). We seek a deformation map $\boldsymbol{y}$, model parameters $\boldsymbol{p}$, and the intensity distributions $\boldsymbol{\phi}$ (mean and covariance of a Gaussian distribution; see below) for the labels $\Theta$. The deformation map $\boldsymbol{y}$ defines the registration between the patient-specific image and the atlas space. The model parameters inverted for are given by $\boldsymbol{p} := \{\boldsymbol{x}_0, \gamma, \kappa_W, T\}$ with predefined initial condition $\pi_{TU}(\boldsymbol{x}, 0) \propto \exp(\| \boldsymbol{x} - \boldsymbol{x}_0 \|_2^2)$, initial seed location $\boldsymbol{x}_0 \in \Omega$, diffusion coefficient $\kappa_W > 0$ for WM, and final time $T > 0$; $\gamma > 0$ determines the strength of the tumor mass effect (see Figure 2 for an illustration). Under the assumption that the conditional probability distribution function of each $\boldsymbol{q}(\boldsymbol{x})$ can be modeled as a weighted mixture of Gaussians, we can solve for $\boldsymbol{\phi}, \boldsymbol{y}, \boldsymbol{p}$ as follows:

$$\underset{\phi, y, p}{\text{maximize}} \prod_{x \in \Omega} \sum_{i \in \Theta} \log(\pi_i(\boldsymbol{y}(\boldsymbol{x}) \mid \boldsymbol{p}) g_i(\boldsymbol{q}(\boldsymbol{x}) \mid \phi)), \quad 4.$$

where $g_i(\boldsymbol{q}(\boldsymbol{x})|\boldsymbol{\phi})$ is a multivariate Gaussian distribution with mean $\boldsymbol{\mu}_i$ and covariance matrix $\boldsymbol{\Sigma}_i$, and $\boldsymbol{\phi} := \{\boldsymbol{\mu}_i, \boldsymbol{\Sigma}_i\}_{i \in \Theta}$. To compute the maximum a posteriori (MAP) estimate of Equation 4, an expectation-maximization approach is considered. The optimization problem is solved using a derivative-free algorithm. We showcase results obtained with GLISTR in Figure 3.

GLISTRboost (96), an extension of GLISTR, is a hybrid generative-discriminative model. The generative model is GLISTR; the discriminative part is based on a voxel-level multi-class classification through a gradient-boosting ensemble model of decision trees (169, 170). It refines the tumor labels obtained from solving Equation 4 based on information from multiple patients. The classifier is trained using the glioma data of the brain tumor segmentation (BraTS) challenge (31–35). Decision trees of maximum depth three are trained in a subset of the data to introduce randomness. A cross-validation framework is used to avoid overfitting. Additional randomness is introduced by sampling stochastically a subset of imaging features at each node. Five features are used for training the discriminative part of GLISTRboost: (*a*) image intensities from individual mpMRI and their differences across all of the datasets, (*b*) first- and second-order image derivative information, (*c*) the geodesic distance transform (171) from an initialized seed-point $\boldsymbol{x}_0$ of the tumor, (*d*) the posterior probability maps $\boldsymbol{\pi}_i$, and (*e*) first- and second-order texture statistics computed from a gray-level co-occurrence matrix. In a last step, each segmentation is refined by assessing the local intensity distribution of the current segmentation labels across each patient's mpMRI scans and updating their spatial configuration based on a Bayesian probabilistic framework (172). Here, the intensity distributions of the WM, ED, NE, and ET are populated, considering the corresponding voxels of tissue probability equal to one. The histograms of the three pair-wise distributions considered [i.e., ED versus WM in T2-FLAIR (T2–fluid-attenuated inversion recovery), ET versus ED in T1-CE (T1–contrast-enhanced), and ET versus NE in T1-CE] are then normalized. The maximum likelihood estimation is then used to model the class-conditional probability densities [$\Pr(I(v_i)|\text{class})$] of each class by a distinct Gaussian function for each class. The voxels of each class in close proximity (offset = 4) to the voxels of the paired class are then iteratively evaluated by assessing their intensity $I(v_i)$ and comparing the $\Pr(I(v_i)|\text{class}_1)$ with $\Pr(I(v_i)|\text{class}_2)$. The voxel $v_i$ is then classified into the class with the larger conditional probability, which is equivalent to a classification based on Bayes' theorem with equal priors for the two classes, i.e., $\Pr(\text{class}_1) = \Pr(\text{class}_2) = 0.5$. GLISTRboost has been evaluated on the testing datasets ($n = 186$) of the BraTS 2015 challenge and ranked as the top-performing method (33, 96).

#### 4.2.2. Scalable Integrated Biophysics-based Image Analysis (SIBIA).—

SIBIA (91, 136, 164, 166) is a novel framework for integrating biophysical simulations with mpMRI and optimization. It is a continuation of our efforts described in References 4, 92, 96, 98, and 159. It addresses several limitations of GLISTR/GLISTRboost, the main one being the need to manually select the tumor seed $\boldsymbol{x}_0$. SIBIA is fully automatic and does not require user intervention. Like GLISTR/GLISTRboost, SIBIA uses (*a*) biophysical models for the tumor-modeling part (116, 122; see also Section 2) and (*b*) the Constrained Large Deformation Diffeomorphic Image Registration (CLAIRE) package (173–175) as a module for diffeomorphic registration. The formulation is in spirit similar to that in Reference 98. We invert for a velocity field $\boldsymbol{v}$ that parameterizes the deformation map $\boldsymbol{y}$ from the patient to

the atlas space and tumor model parameters $\boldsymbol{p}$ using a PDE-constrained formulation of the form (91)

$$\underset{p,v,m,c}{\text{minimize}} \frac{1}{2}\int_{\Omega}(c_{\mathrm{A}}(\boldsymbol{x},1)-c_{\mathrm{P}}(\boldsymbol{x},1))^2\dot{x}+\frac{1}{2}\int_{\Omega}\|\boldsymbol{m}_{\mathrm{A}}(\boldsymbol{x},1)-\boldsymbol{m}_{\mathrm{P}}(\boldsymbol{x},1)\|_2^2\dot{x}+\mathscr{R}(\boldsymbol{p},\boldsymbol{v}) \quad 5a.$$

$$\text{subject to } \mathscr{F}_T(c,\boldsymbol{m},\boldsymbol{v},\boldsymbol{p})=0,\ \mathscr{F}_R(c,\boldsymbol{m},\boldsymbol{v})=0. \quad 5b.$$

This model is a direct extension of the formulations in Section 3. The functions $c_{\mathrm{A}}(\boldsymbol{x}, 1)$, $c_{\mathrm{P}}(\boldsymbol{x}, 1)$, $\boldsymbol{m}_{\mathrm{A}}(\boldsymbol{x}, 1)$, and $\boldsymbol{m}_{\mathrm{P}}(\boldsymbol{x}, 1)$ are tumor and tissue probability maps defined in the patient (P) and atlas (A) space. The data input to the inverse problem are estimates for (*a*) patient-specific tumor probabilities $c_{\mathrm{OBS}}$: $\Omega \rightarrow [0, 1]$; (*b*) patient-specific material properties $\boldsymbol{m}_{\mathrm{OBS}}$ : $\Omega \rightarrow [0, 1]^3$, $\boldsymbol{m}_{\mathrm{OBS}}(\boldsymbol{x}) := (\boldsymbol{\pi}_{\mathrm{OBS,W}}(\boldsymbol{x}), \boldsymbol{\pi}_{\mathrm{OBS,G}}(\boldsymbol{x}), \boldsymbol{\pi}_{\mathrm{OBS,F}}(\boldsymbol{x}))$ (patient geometry); and (*c*) the tumor-free patient geometry (the atlas image) $\boldsymbol{m}_{\mathrm{ATL}} : \Omega \rightarrow [0, 1]^3$, $\boldsymbol{m}_{\mathrm{ATL}}(\boldsymbol{x}) := (\boldsymbol{\pi}_{\mathrm{ATL,W}}(\boldsymbol{x}), \boldsymbol{\pi}_{\mathrm{ATL,G}}(\boldsymbol{x}), \boldsymbol{\pi}_{\mathrm{ATL,F}}(\boldsymbol{x}))$ (atlas geometry). The operator $\mathscr{F}_T$ is the forward tumor model (see Equation 2 for an example); $\mathscr{F}_T$ is used to predict a tumor in the atlas space that best matches the patient's tumor. The operator $\mathscr{F}_R$ is the forward registration model (a hyperbolic transport equation); it is used to map the patient data to the atlas space. The inputs to the forward registration operator $\mathscr{F}_R$ are the patient-specific tumor and tissue probabilities $c_{\mathrm{OBS}}(\boldsymbol{x})$ and $\boldsymbol{m}_{\mathrm{OBS}}(\boldsymbol{x})$, respectively.

Formally, our scheme proceeds as follows: Given some trial tumor parameter $\boldsymbol{p}$, the forward tumor model $\mathscr{F}_T$ produces the predicted tumor probabilities $c_{\mathrm{A}}(\boldsymbol{x}, 1)$ and tissue probability maps $\boldsymbol{m}_{\mathrm{A}}(\boldsymbol{x}, 1) = (\boldsymbol{\pi}_{1,\mathrm{W}}(\boldsymbol{x}), \boldsymbol{\pi}_{1,\mathrm{G}}(\boldsymbol{x}), \boldsymbol{\pi}_{1,\mathrm{F}}(\boldsymbol{x}))$ at time $t = 1$ in the atlas space, where $\boldsymbol{\pi}_{1,j}(\boldsymbol{x}) := \boldsymbol{\pi}_{\mathrm{ATL},\,j}(\boldsymbol{x})(1 - c_{\mathrm{A}}(\boldsymbol{x}, 1))$, $j \in \{\mathrm{W}, \mathrm{G}, \mathrm{F}\}$ are the updated probability maps for WM, GM, and CSF (healthy brain anatomy). Given some trial velocity field $\boldsymbol{v}(\boldsymbol{x})$, the forward registration model $\mathscr{F}_R$ generates a spatially transformed representation $c_{\mathrm{P}}(\boldsymbol{x}, 1)$ and $\boldsymbol{m}_{\mathrm{P}}(\boldsymbol{x}, 1)$ at pseudotime $t = 1$ of the patient-specific data $c_{\mathrm{OBS}}(\boldsymbol{x})$ and $\boldsymbol{m}_{\mathrm{OBS}}(\boldsymbol{x})$. In the inverse problem shown in Equation 5, we seek control variables $\boldsymbol{p}$ and $\boldsymbol{v}$ such that the tumor and tissue probability maps $c_{\mathrm{A}}(\boldsymbol{x}, 1)$, $c_{\mathrm{P}}(\boldsymbol{x}, 1)$, $\boldsymbol{m}_{\mathrm{A}}(\boldsymbol{x}, 1)$, and $\boldsymbol{m}_{\mathrm{P}}(\boldsymbol{x}, 1)$ defined in the atlas and patient space are as close as possible. We measure the proximity between these data using a squared $L^2$ distance in Equation 5. The functional $\mathscr{R}$ in Equation 5 is a regularization model for the control variables $\boldsymbol{p}$ and $\boldsymbol{v}$.

Computing the minimizer of Equation 5 is conceptually equivalent to computing the MAP point for Equation 4. In SIBIA, we invert for the growth rate $\rho > 0$, the diffusivity $\kappa > 0$ and/or the initial condition $c_0(\boldsymbol{x})$, where $c_0(\boldsymbol{x}) := \sum_{k=1}^{r} w_k \phi_k(\boldsymbol{x})$ is modeled as an $r$-dimensional space spanned by Gaussian basis functions $\phi_k : \Omega \rightarrow \mathbb{R}$. This parameterization allows us to model multi-focal and multi-centric tumors. SIBIA (91, 136, 164, 166) uses a globalized, adjoint-based method (i.e., derivatives of the Lagrangian). We do not iterate on both control variables $\boldsymbol{v}$ and $\boldsymbol{p}$ simultaneously. We perform a block elimination instead, and iterate, resulting in an interleaved optimization on the controls exploiting dedicated solvers

for the individual subblocks (116, 136, 173, 175). SIBIA has been deployed in parallel computing platforms to further amortize computational costs (136, 174, 175).

We have applied SIBIA to hundreds of real 3D datasets and achieved encouraging results for atlas-based segmentation (91, 166). However, our initial scheme (91) does not allow reliable inversion for meaningful model parameter $\boldsymbol{p}$; its predictive capabilities are limited. One key issue is that we map the patient geometry to the atlas space. In our most recent work (164), we have changed the formulation to map the atlas geometry to the patient space, excluding tumor probabilities. We hypothesize [and have demonstrated experimentally through synthetic test problems (164)] that this improved scheme—in combination with a sparsity soft constraint for the parameterization of the initial condition (137)—allows us to more reliably invert for patient-specific tumor parameters.

## 5. CLINICALLY RELEVANT STUDIES

Numerous clinically relevant studies revolve around precision diagnostics (176) leveraging rich information from biophysical models of tumor growth (177). Considering the complexity of routinely acquired advanced mpMRI of GBM patients (178), there is an apparent need for advanced computational algorithms for automated image analyses. Such analyses include automated brain tumor segmentation algorithms coupled with biophysical growth models (4, 91, 96, 149, 164, 167, 179–181; see also Section 4) leading to an accurate quantitative assessment of the distinct histologically heterogeneous tumor subregions, potentially benefiting the clinical workflow in radiology and radiation oncology settings, as well as providing platforms for radio(geno)mic research. Numerous examples in the literature indicate the benefit of biophysical tumor growth modeling for robust patient-specific tumor characterization (i.e., personalized medicine), especially by virtue of accurate population-based spatial distribution atlases of GBM (158).

We appreciate the potential benefit of incorporating biophysical modeling in clinical research studies. To facilitate the widespread use of biophysical modeling, we have already integrated GLISTR and GLISTRboost into the extended suite of the *Cancer Imaging Phenomics Toolkit* (CaPTk) (182, 183) and made them available for public use through the online *Image Processing Portal* (IPP; see https://ipp.cbica.upenn.edu) of the Center for Biomedical Image Computing and Analytics (CBICA; see https://www.cbica.upenn.edu). CBICA's IPP allows users to perform their analyses without any software installation through CBICA's computing resources. The integration of CLAIRE and SIBIA with CaPTk is an ongoing project. The sections below summarize a few example studies relating radiographic analyses to specific endpoints (e.g., clinical outcome, molecular characteristics) and do not intend to be a complete literature review.

### 5.1. Prediction of Patient Overall Survival

Patient overall survival (OS) is the ultimate clinical outcome; accurate predictions could affect clinical decision making and treatment planning. Numerous studies have been focusing on GBM prognostic evaluation and stratification. These studies support the benefit of incorporating biophysical growth models (67, 68, 70, 80, 85, 184); show the generalization across multi-institutional data (185, 186), even when the models are

compared with the prognostic value of current clinical and genomic markers; and demonstrate that an integration of models with imaging offers additive prognostic value even beyond the current WHO classification (69, 70, 187) (see Figure 4). Furthermore, integration of biophysical growth modeling with advanced radio-phenotypical features derived from basic structural mpMRI (i.e., T1, T1-CE, T2, T2-FLAIR) can compensate for the lack of advanced mpMRI scans (e.g., dynamic susceptibility contrast MRI, diffusion tensor imaging) and still offer comparable prognostic predictions (59).

### 5.2. Treatment Planning

Although more than 90% of tumor recurrence occurs within ED (188), there is limited research focused on its assessment and its microenvironment (189). ED appears to develop in response to angiogenic and vascular permeability factors associated with infiltrating tumor (190). As tumors outgrow the native blood supply, the resultant ischemia triggers further secretion of angiogenic factors that promote vascular proliferation (191, 192). Advanced computational analyses, incorporating biophysical tumor growth modeling, have been conducted to evaluate the amount of heterogeneous tumor infiltration in the ED and thus assess the risk of recurrence (61, 64, 66). The value of these studies has been retrospectively validated in independent discovery and replication cohorts with significant results (odds ratio >13). Furthermore, these assessments were recognized for their usefulness as potential therapeutic tools and are currently in a clinical trial for targeted personalized dose escalation planning.

Along the same lines, various other studies have attempted to shed light on the quantification of microscopic tumor invasion and cell proliferation (193, 194), and also tumor growth rates in relation to diffusion (195), while incorporating growth modeling.

### 5.3. Radiogenomics: Noninvasive Tumor Molecular Characterization

Current tumor molecular characterization is based on ex vivo tissue analysis that cannot capture the tumor's spatial heterogeneity. Since radiographic imaging is routinely acquired and can capture the whole tumor extent, multiple studies have focused on noninvasive prediction of molecular characteristics of GBM from radiographic tumor patterns (19) while incorporating biophysical growth modeling; examples of these studies include (*a*) genome-wide association analysis with tumor spatial distribution patterns (15), (*b*) prediction of individual molecular characteristics (20, 21, 23, 24, 27), and (*c*) prediction of transcriptomic GBM subtypes (67, 196). Below, we discuss a few example studies focusing on noninvasive prediction of some of the most important GBM molecular characteristics: the isocitrate dehydrogenase-1 (IDH1), the O6-methylguanine DNA methyltransferase (MGMT), and the epidermal growth factor receptor variant III (EGFRvIII).

According to the 2016 WHO classification (6), determination of the IDH1 mutational status is essential for the clinical diagnosis and treatment planning of glioma. The ability to identify IDH1 at initial patient presentation can influence decision making and appropriate treatment planning. Furthermore, as IDH1 mutant (IDH1-mut) enzyme inhibitors and immunotherapeutic options are developed, noninvasive determination at preoperative and follow-up time points can be influential. With that in mind, a preoperative noninvasive

signature of IDH1 was constructed on the basis of quantitative radiographic phenotypical features from a retrospective cohort of 86 high-grade glioma mpMRI scans (IDH1-mut:15) (24). The features integrated volumetric and morphological measurements, texture descriptors, location characteristics, and biophysical growth model parameters (96). Following multivariate cross-validated forward-sequential feature selection, 61 of these features were identified as the most discriminative, primarily including texture descriptors and a distinct spatial location of the IDH1-mut tumors with more prominence in the frontal/occipital lobe. Quantitative evaluation of this signature yielded an accuracy of 88.4% [sensitivity = 66.7%, specificity = 92.9%, area under the curve (AUC) = 0.81] on classifying IDH1 mutational status.

MGMT promoter methylation is another well-accepted prognostic indicator in GBM that directly influences the effectiveness of chemotherapy, where specifically methylated tumors (MGMT+) are more responsive. A noninvasive signature for the status of the MGMT promoter methylation could contribute in addressing limitations of the current determination, which can be limited by inadequate tissue specimen or assay failures. Rathore et al. (20, 21) identified a retrospective cohort of 122 patients diagnosed with pathology-proven de novo GBM (MGMT+: 46) and available preoperative mpMRI scans. They extracted 330 radiographic phenotypical features per patient, including measurements of volume, morphology, texture, and voxel-wise location characteristics obtained after incorporating a biophysical model (96).

Multivariate cross-validated forward sequential feature selection identified 46 features as the ones to create the noninvasive signature, which revealed that MGMT+ tumors have lower neo-vascularization and cell density than MGMT-unmethylated tumors. Assessment of the location characteristics yielded a distinctive spatial pattern, with the MGMT+ tumors being lateralized to the left hemisphere compared with MGMT-unmethylated tumors. The cross-validated accuracy of this signature in correctly classifying MGMT+ tumors was 84.43% (sensitivity = 80.43%, specificity = 86.84%, AUC = 0.85).

Another GBM driver mutation is EGFRvIII, which has been considered in multiple GBM clinical trials. It was recently discovered that glioblastomas harboring the mutation have a distinct spatial distribution pattern when compared to tumors without the mutation, which could distinguish a mutant tumor with 75% accuracy (27). Figure 5 shows the voxel-wise location prominence of GBM, in spatial distribution atlases relating to the presence/absence of the EGFRvIII mutation, after incorporating biophysical modeling (96). A preexisting study, which evaluated the location prominence of GBM stratified by EGFRvIII status *without* incorporating biophysical modeling parameters in the image analysis, obtained different results (16). Notably, the studies that incorporated biophysical modeling (23, 27) evaluated a three-times-larger sample, which is expected to potentially provide more robust statistics of spatial patterns.

### 5.4. Generating Hypotheses for Further Investigation

Integrated analysis of advanced mpMRI scans and biophysical modeling (96) has contributed to the discovery of a potential molecular target, presenting an opportunity for potential therapeutic development (22, 25). Radiographic signatures of EGFR extracellular

domain missense mutants (i.e., A289V) were identified, suggestive of an invasive and proliferative phenotype (25) associated with shorter survival in patients. These findings were corroborated by experiments in vitro and in vivo (animal models). Kaplan-Meier survival curves comparing mice implanted with modified cell lines in vivo (i.e., U87 and HK281 tumor cell lines expressing either wild-type EGFR or the EGFR A289V mutant—$n = 6$ per group, $p < 0.01$) demonstrated decreased OS, increased proliferation, and increased invasion. Further, mechanistic exploration revealed increased MMP1 expression (driven by ERK activation) leading to both increased proliferation and invasion. Finally, the tumor driver status of EGFR A289V was demonstrated by in vivo targeting via an EGFR monoclonal antibody (mAb806), increasing animal survival and inhibiting tumor growth. These results serve to highlight the complexity of the EGFR signaling cascade and pathway nuances of extracellular domain mutations in the context of cancer (25). Figure 6 summarizes the results of this study (25).

## 6. CONCLUSIONS

We have reviewed existing approaches toward integration of computational models and image analysis for characterization of neuroimaging data of brain tumor patients. We have described state-of-the-art technology for biophysical tumor growth modeling, as well as the inverse problem of estimating adequate parameters to fit the model output to available observations. We have discussed the integration of biophysical models with image analysis algorithms and showcased clinically relevant results that demonstrate the benefit of such an integration.

Despite these encouraging results, we note that a successful integration of biophysical models with image analysis poses significant mathematical and computational challenges. First and foremost, biological systems involve complex, multifaceted, heterogeneous biological, physical, and chemical behavior at different spatial and temporal scales of observation (78). This makes the development of predictive models a difficult endeavor. Complex models result in a vast number of parameters (78, 104), which makes them difficult to calibrate to medical imaging data, especially since clinical data provide only scarce information (e.g., single time point; imaging noise; low resolution; only indirect phenotypic measurements reflecting coarse aspects of these complex underlying biological processes). Aside from computational issues, additional mathematical and modeling issues make such an integration even more difficult; these include (*a*) uncertainties in the data and model, (*b*) modeling errors and inadequate mathematical models, (*c*) ill-posedness of the inverse problems (nonuniqueness of the solution), (*d*) decisions about appropriate regularization models and data misfit terms, and/or (*e*) influences of the numerical discretization on the inversion. Consequently, other sources of information or, equivalently, strong modeling priors need to be integrated to make these approaches practical. One possibility to alleviate some of these challenges, and to define, test, analyze, and design appropriate priors, is through animal models or in vitro studies, although this approach is known to be limited, as well, in its ability to generalize to in vivo cancer growth in humans.

Ample and diverse data are expected to contribute toward addressing these challenges and expedite further developments in biophysical modeling of the growth, invasion, and

proliferation of untreated gliomas, as well as models of polyclonal gliomas following chemotherapy and surgical resection. Such data exist only across institutions, and the current paradigm for multi-institutional collaborations (i.e., pooling data in a centralized location) suffers from various privacy, technical, and ownership concerns. However, existing efforts on alternative collaboration paradigms based on distributed learning approaches (197, 198) could be investigated further to address the need for large datasets, while overcoming data-ownership concerns.

Integrated diagnostics increasingly demonstrate their clinical importance, with the most recent clinical example of the revised 2016 WHO classification for CNS tumors incorporating molecular characterization to histologic patterns (6). However, several intrinsic and extrinsic factors hinder this molecular characterization, which currently requires ex vivo invasive tissue analysis. Such analysis is limited in assessing the tumor's spatial heterogeneity and not amenable to relatively regularly repeated evaluations during treatment. In contrast, mpMRI can noninvasively provide a macroscopic radiographic phenotype capturing the whole extent of a tumor. Since mpMRI scans of GBM patients are part of clinical routine (preoperatively and longitudinally during adjuvant treatment), there is an opportunity for ample data to be utilized for developing dynamic noninvasive biomarkers. Our working hypothesis is that the integration of these data with sophisticated computational tools is beneficial for assessing the spatial and temporal heterogeneity of GBM and has the potential to influence treatment, improving the health of GBM patients.

There is a notable growth of literature related to integrated radio-phenotypical diagnostics revolving around precision diagnostics, i.e., the precise molecular characterization of tumors, by looking for patterns and targets identified from a population of patients. However, such noninvasive macroscopic integration, instead of revolving solely around precision medicine, could also contribute to personalized/adaptive approaches that may expand on precision medicine by characterizing within-patient heterogeneity, spatially and temporally. Personalized/adaptive medicine may have the potential to further customize treatment options using patient-specific factors. As tumor growth and invasion models become more elaborate, they might play a role in allowing clinicians to estimate patient-specific growth parameters that contribute to a more precise characterization of tumor properties.

Recent computational studies have provided evidence of noninvasive comprehensive multi-scale characterization of a tumor's phenotype, behavior, and microenvironment before, during, and after treatment, thereby offering important information for diagnostic, prognostic, and predictive purposes, while capturing the whole extent and heterogeneity of the tumor. Integrated radio-phenotypical biomarkers may enable opportunities for noninvasive patient selection for targeted therapy, stratification into clinical trials, prognosis, and repeatable monitoring of molecular characteristics during the treatment course, leading to quantitative noninvasive evaluation of treatment response. Such advancements in integrated diagnostics, describing a composite multiscale index through synergistic analyses of radiographic, histopathologic, genetic, clinical, and biophysical data, may speed up scientific discovery and improve both precision medicine and personalized/adaptive medicine.

Based on current results, we are convinced that the integration of advanced computational, mathematical, and biophysical methods offers great promise to become an indispensable and influential tool for patient management. However, we acknowledge that a significant amount of multidisciplinary work lies ahead. Pending further clinical validation, we anticipate the integration of these tools into a future iteration of the WHO classification scheme for CNS tumors, thus providing a more complete understanding of the mechanisms of disease, leading to more effective treatment and beneficial patient prospects.

## ACKNOWLEDGMENTS

This work was partly supported by the Simons Foundation (586055); the National Institutes of Health (5R01NS042645-14, R01NS042645, U24CA189523, UL1TR001878); the Institute for Translational Medicine and Therapeutics at the University of Pennsylvania; the National Science Foundation (CCF-1817048, CCF-1725743, DMS-1854853); the US Department of Energy, Office of Science, Office of Advanced Scientific Computing Research, Applied Mathematics program (DE-SC0019393); and the US Air Force Office of Scientific Research (FA9550-17-1-0190). Computing time on the Texas Advanced Computing Centers (TACC) systems was provided by an allocation from TACC and the NSF.

## Glossary

**CNS**
central nervous system

**GBM**
glioblastoma multiforme

**mpMRI**
multi-parametric magnetic resonance imaging

**WHO**
World Health Organization

**Radiography**
imaging technique using radiation to expose the internal structure of an object

**Pathophysiology**
the disordering of physiological processes in an organism due to disease or injury

**Radiomics**
extraction of features from radiographic medical images

**Morphologichistopathologic characterization**
characterization of a disease based on the morphology of tissue cells assessed in microscopic examination of histopathology slides

**Molecularcytogenetic characterization**
characterization of a disease based on the assessment of its molecular profiling

**Pseudoprogression**
growth of tumor size in response to treatment rather than disease progression

**Polyclonal tumor**
tumor arising from the division of multiple mutated cells, as opposed to a single mutation

**WM**
white matter

**GM**
gray matter

**ED**
edematous/tumor-infiltrated tissue

**CSF**
cerebrospinal fluid

**TU region**
tumor core region

**ET region**
enhancing tumor region

**NE region**
necrotic and nonenhancing tumor region

**OS**
overall survival

## LITERATURE CITED

1. Collins VP. 1998 Gliomas. Cancer Surv. 32:37–51 [PubMed: 10489622]
2. Holland EC. 2000 Glioblastoma multiforme: the terminator. PNAS 97:6242–44 [PubMed: 10841526]
3. Mang A, Gholami A, Davatizkos C, Biros G. 2018 PDE-constrained optimization in medical image analysis. Optim. Eng 19(3):765–812
4. Gooya A, Pohl KM, Bilello M, Cirillo L, Biros G, et al. 2013 GLISTR: glioma image segmentation and registration. IEEE Trans. Med. Imaging 31:1941–54
5. Kleihues P, Burger PC, Scheithauer BW. 1993 The new WHO classification of brain tumours. Brain Pathol. 3:255–68 [PubMed: 8293185]
6. Louis DN, Perry A, Reifenberger G, von Deimling A, Figarella-Branger D, et al. 2016 The 2016 World Health Organization classification of tumors of the central nervous system: a summary. Acta Neuropathol. 131:803–20 [PubMed: 27157931]
7. Thust SC, van den Bent MJ, Smits M. 2018 Pseudoprogression of brain tumors. J. Magnet. Reson. Imaging 48:571–89
8. Jaffe CC. 2012 Imaging and genomics: Is there a synergy? Radiology 264:329–31 [PubMed: 22821693]
9. Rutman AM, Kuo MD. 2009 Radiogenomics: creating a link between molecular diagnostics and diagnostic imaging. Eur. J. Radiol 70:232–41 [PubMed: 19303233]
10. Mazurowski MA. 2015 Radiogenomics: what it is and why it is important. J. Am. Coll. Radiol 12:862–66 [PubMed: 26250979]

11. Zinn PO, Majadan B, Sathyan P, Singh SK, Majumder S, et al. 2011 Radiogenomic mapping of edema/cellular invasion MRI-phenotypes in glioblastoma multiforme. PLOS ONE 6(10):e25451 [PubMed: 21998659]
12. Gevaert O, Mitchell LA, Achrol AS, Xu J, Echegaray S, et al. 2014 Glioblastoma multiforme: exploratory radiogenomic analysis by using quantitative image features. Radiology 273:168–74 [PubMed: 24827998]
13. Jain R, Poisson LM, Gutman D, Scarpace L, Hwang SN, et al. 2014 Outcome prediction in patients with glioblastoma by using imaging, clinical, and genomic biomarkers: focus on the nonenhancing component of the tumor. Radiology 272:484–93 [PubMed: 24646147]
14. Itakura H, Achrol AS, Mitchell LA, Loya JJ, Liu T, et al. 2015 Magnetic resonance image features identify glioblastoma phenotypic subtypes with distinct molecular pathway activities. Sci. Transl. Med 7:303ra138
15. Elsheikh SSM, Bakas S, Mulder NJ, Chimusa ER, Davatzikos C, Crimi A. 2018 Multi-stage association analysis of glioblastoma gene expressions with texture and spatial patterns In Brainlesion: Glioma, Multiple Sclerosis, Stroke and Traumatic Brain Injuries. BrainLes 2018, ed. Crimi A, Bakas S, Kuijf H, Keyvan F, Reyes M, Walsum T van, pp. 239–50. Lecture Notes in Computer Science, Vol. 11383 Cham, Switz.: Springer
16. Ellingson B, Lai A, Harris R, Selfridge J, Yong W, et al. 2013 Probabilistic radiographic atlas of glioblastoma phenotypes. Am. J. Neuroradiol 34:533–40 [PubMed: 22997168]
17. Bakas S, Akbari H, Pisapia J, Martinez-Lage M, Rozycki M, et al. 2017 In vivo detection of EGFRvIII in glioblastoma via perfusion magnetic resonance imaging signature consistent with deep peritumoral infiltration: the $\phi$-Index. Clin. Cancer Res 23:4724–34 [PubMed: 28428190]
18. Bakas S, Binder ZA, Akbari H, Martinez-Lage M, Rozycki M, et al. 2016 Highly-expressed wild-type EGFR and EGFRvIII mutant glioblastomas have similar MRI signature, consistent with deep peritumoral infiltration. Neuro-Oncology 18:vi125–vi126
19. Rathore S, Bakas S, Akbari H, Nasrallah M, Bagley S, Davatzikos C. 2019 Machine learning radiomic biomarkers non-invasively assess genetic characteristics of glioma patients. Cancer Res. 79(13 Suppl.):1392
20. Rathore S, Bakas S, Nasrallah M, Akbari H, Bagley S, et al. 2018 Multivariate pattern analysis of de novo glioblastoma patients offers in vivo evaluation of O6-methylguanine-DNA-methyltransferase (MGMT) promoter methylation status, compensating for insufficient specimen and assay failures. Neuro-Oncology 20:vi186
21. Rathore S, Bakas S, Nasrallah M, Bagley S, Akbari H, et al. 2018 Non-invasive determination of the O6-methylguanine-DNA-methyltransferase (MGMT) promoter methylation status in glioblastoma (GBM) using magnetic resonance imaging (MRI). J. Clin. Oncol 36(15 Suppl.):2051
22. Binder Z, Bakas S, Wileyto EP, Akbari H, Rathore S, et al. 2016 Extracellular EGFR289 activating mutations confer poorer survival and suggest enhanced motility in primary GBMs. Neuro-Oncology 18:105–6 [PubMed: 26409568]
23. Bakas S, Akbari H, Pisapia J, Rozycki M, O'Rourke DM, Davatzikos C. 2015 Identification of imaging signatures of the epidermal growth factor receptor variant III (EGFRvIII) in glioblastoma. Neuro-Oncology 17:v154
24. Bakas S, Rathore S, Nasrallah M, Akbari H, Binder Z, et al. 2018 Non-invasive in vivo signature of IDH1 mutational status in high grade glioma, from clinically-acquired multi-parametric magnetic resonance imaging, using multivariate machine learning. Neuro-Oncology 20:vi184–vi185
25. Binder ZA, Thorne AH, Bakas S, Wileyto EP, Bilello M, et al. 2018 Epidermal growth factor receptor extracellular domain mutations in glioblastoma present opportunities for clinical imaging and therapeutic development. Cancer Cell 34:163–77 [PubMed: 29990498]
26. Beig N, Patel J, Prasanna P, Hill V, Gupta A, et al. 2018 Radiogenomic analysis of hypoxia pathway is predictive of overall survival in glioblastoma. Sci. Rep 8(1):7 [PubMed: 29311558]
27. Akbari H, Bakas S, Pisapia JM, Nasrallah MP, Rozycki M, et al. 2018 In vivo evaluation of EGFRvIII mutation in primary glioblastoma patients via complex multiparametric MRI signature. Neuro-Oncology 20:1068–79 [PubMed: 29617843]

28. Clark K, Vendt B, Smith K, Freymann J, Kirby J, et al. 2013 The Cancer Imaging Archive (TCIA): maintaining and operating a public information repository. J. Digit. Imaging 26:1045–57 [PubMed: 23884657]
29. Scarpace L, Mikkelsen T, Cha S, Rao S, Tekchandani S, et al. 2016 Cancer Genome Atlas glioblastoma multiforme (TCGA-GBM) data collection. Cancer Imaging Archive. https://wiki.cancerimagingarchive.net/display/Public/TCGA-GBM
30. Pedano N, Flanders A, Scarpace L, Mikkelsen T, Eschbacher J, et al. 2016 Cancer Genome Atlas low grade glioma (TCGA-LGG) data collection. Cancer Imaging Archive. https://wiki.cancerimagingarchive.net/display/Public/TCGA-LGG
31. Bakas S, Reyes M, Jakab A, Bauer S, Rempfler M, et al. 2018 Identifying the best machine learning algorithms for brain tumor segmentation, progression assessment, and overall survival prediction in the BRATS challenge. arxiv:1811.02629 [cs.CV]
32. Bakas S, Akbari H, Sotiras A, Bilello M, Rozycki M, et al. 2017 Advancing the Cancer Genome Atlas glioma MRI collections with expert segmentation labels and radiomic features. Nat. Sci. Data 4:170117
33. Menze BH, Jakab A, Bauer S, Kalpathy-Cramer J, Farahani K, et al. 2015 The multimodal brain tumor image segmentation benchmark (BRATS). IEEE Trans. Med. Imaging 34:1993–2024 [PubMed: 25494501]
34. Bakas S, Akbari H, Sotiras A, Bilello M, Rozycki M, et al. 2017 Segmentation labels and radiomic features for the pre-operative scans of the TCGA-GBM collection. Cancer Imaging Archive. 10.7937/K9/TCIA.2017.KLXWJJ1Q
35. Bakas S, Akbari H, Sotiras A, Bilello M, Rozycki M, et al. 2017 Segmentation labels and radiomic features for the pre-operative scans of the TCGA-LGG collection. Cancer Imaging Archive. 10.7937/K9/TCIA.2017.GJQ7R0EF
36. Simpson AL, Antonelli M, Bakas S, Bilello M, Farahani K, et al. 2019 A large annotated medical image dataset for the development and evaluation of segmentation algorithms. arXiv:1902.09063 [cs.CV]
37. Clatz O, Sermesant M, Bondiau PY, Delingette H, Warfield SK, et al. 2005 Realistic simulation of the 3D growth of brain tumors in MR images coupling diffusion with biomechanical deformation. IEEE Trans. Med. Imaging 24:1334–46 [PubMed: 16229419]
38. Hogea C, Biros G, Abraham F, Davatzikos C. 2007 A robust framework for soft tissue simulations with application to modeling brain tumor mass effect in 3D MR images. Phys. Med. Biol 52:6893–908 [PubMed: 18029982]
39. Yankeelov TE, Atuegwu N, Hormuth D, Weis JA, Barnes SL, et al. 2013 Clinically relevant modeling of tumor growth and treatment response. Sci. Transl. Med 5:187ps9
40. Konukoglu E, Clatz O, Bondiau PY, Delingette H, Ayache N. 2010 Extrapolating glioma invasion margin in brain magnetic resonance images: suggesting new irradiation margins. Med. Image Anal 14:111–25 [PubMed: 20042359]
41. Rockne R, Rockhill JK, Mrugala M, Spence AM, Kalet I, et al. 2010 Predicting the efficacy of radiotherapy in individual glioblastoma patients in vivo: a mathematical modeling approach. Phys. Med. Biol 55:3271–85 [PubMed: 20484781]
42. Ivkovic S, Beadle C, Noticewala S, Massey SC, Swanson KR, et al. 2012 Direct inhibition of myosin II effectively blocks glioma invasion in the presence of multiple motogens. Mol. Biol. Cell 23:533–42 [PubMed: 22219380]
43. Miga M, Paulsen K, Kennedy F, Hoopes J, Hartov A, Roberts D. 1998 Initial in-vivo analysis of 3D heterogeneous brain computations for model-updated image-guided neurosurgery In Proceedings of Medical Image Computing and Computer-Assisted Intervention. MICCAI'98, ed. Wells WM, Colchester A, Delp S, pp. 743–52. Berlin/Heidelberg: Springer
44. Lipkova J, Angelikopoulos P, Wu S, Alberts E, Wiestler B, et al. 2019 Personalized radiotherapy design for glioblastoma: integrating mathematical tumor models, multimodal scans, and Bayesian inference. IEEE Trans. Med. Imaging 38:1875–84 [PubMed: 30835219]
45. Chen X, Summers RM, Yoa J. 2012 Kidney tumor growth prediction by coupling reaction-diffusion and biomechanical model. IEEE Trans. Biomed. Eng 60:169–73 [PubMed: 23047857]

46. Wong KCL, Summers RM, Kebebew E, Yao J. 2015 Tumor growth prediction with reaction-diffusion and hyperelastic biomechanical model by physiological data fusion. Med. Image Anal 25:72–85 [PubMed: 25962846]
47. Wong KCL, Summers RM, Kebebew E, Yoa J. 2017 Pancreatic tumor growth prediction with elastic-growth decomposition, image-derived motion, and FDM-FEM coupling. IEEE Trans. Med. Imaging 36:111–23 [PubMed: 27529869]
48. Garcia-Cremades M, Pitou C, Iversen PW, Troconiz IF. 2018 Predicting tumour growth and its impact on survival in gemcitabine-treated patients with advanced pancreatic cancer. Eur. J. Pharm. Sci 115:296–303 [PubMed: 29366960]
49. Filipovic N, Djukic T, Saveljic I, Milenkovic P, Jovicic G, Djuric M. 2014 Modeling of liver metastatic disease with applied drug therapy. Comput. Methods Programs Biomed 115:162–70 [PubMed: 24831076]
50. Tariq I, Humbert-Vidan L, Chen T, South CP, Ezhil V, et al. 2015 Mathematical modelling of tumour volume dynamics in response to stereotactic ablative radiotherapy for non-small cell lung cancer. Phys. Med. Biol 60:3695–713 [PubMed: 25884575]
51. Mi H, Petitjean C, Dubray B, Vera P, Ruan S. 2014 Prediction of lung tumor evolution during radiotherapy in individual patients with PET. IEEE Trans. Med. Imaging 33:995–1003 [PubMed: 24710167]
52. Prapidkumar KK, Manojbhai DD, Rajamenakshi R. 2016 Prediction analysis for tumor growth from large scale non-invasive image In 2016 IEEE International Conference on Recent Trends in Electronics, Information and Communication Technology (RTEICT), Bangalore, pp. 366–70. Piscataway, NJ: IEEE
53. Atuegwu NC, Colvin DC, Loveless ME, Xu L, Gore JC, Yankeelov TE. 2012 Incorporation of diffusion-weighted magnetic resonance imaging data into a simple mathematical model of tumor growth. Phys. Med. Biol 57:225–40 [PubMed: 22156038]
54. Roque T, Risser L, Kersemans V, Smart S, Allen D, et al. 2018 A DCE-MRI driven 3-D reaction-diffusion model of solid tumor growth. IEEE Trans. Med. Imaging 37:724–32 [PubMed: 29533893]
55. Hand L, Hipwell JH, Eiben B, Barratt D, Modat M, et al. 2014 A nonlinear biomechanical model based registration method for aligning prone and supine MR breast images. IEEE Trans. Med. Imaging 33:682–94 [PubMed: 24595342]
56. Lorenzo G, Scott MA, Tew K, Hughes TJR, Zhang YJ, et al. 2016 Tissue-scale, personalized modeling and simulation of prostate cancer growth. PNAS 113:E7663–E7671 [PubMed: 27856758]
57. Gutman DA, Cooper LAD, Hwang SN, Holder CA, Gao J, et al. 2013 MR imaging predictors of molecular profile and survival: multi-institutional study of the TCGA glioblastoma data set. Radiology 267:560–69 [PubMed: 23392431]
58. Mazurowski MA, Desjardins A, Malof JM. 2013 Imaging descriptors improve the predictive power of survival models for glioblastoma patients. Neuro-Oncology 15:1389–94 [PubMed: 23396489]
59. Bakas S, Shukla G, Akbari H, Sotiras A, Erus G, et al. 2017 Accurate and generalizable pre-operative prognostic stratification of glioblastoma patients using integrative quantitative radiomic analysis of conventional MRI. Neuro-Oncology 19:vi151
60. Bonekamp D, Deike K, Wiestler B, Wick W, Bendszus M, et al. 2015 Association of overall survival in patients with newly diagnosed glioblastoma with contrast-enhanced perfusion MRI: comparison of intraindividually matched T1- and T2*-based bolus techniques. J. Magn. Reson. Imaging 42:87–96 [PubMed: 25244574]
61. Akbari H, Macyszyn L, Da X, Wolf RL, Bilello M, et al. 2014 Pattern analysis of dynamic susceptibility contrast-enhanced MR imaging demonstrates peritumoral tissue heterogeneity. Radiology 273:502–10 [PubMed: 24955928]
62. Nicolasjilwan M, Hu Y, Yan C, Meerzaman D, Holder CA, et al. 2015 Addition of MR imaging features and genetic biomarkers strengthens glioblastoma survival prediction in TCGA patients. J. Neuroradiol 42:212–21 [PubMed: 24997477]

63. Velazquez ER, Meier R, Dunn WD Jr., Alexander B, Wiest R, et al. 2015 Fully automatic GBM segmentation in the TCGA-GBM dataset: prognosis and correlation with VASARI features. Sci. Rep 5:16822 [PubMed: 26576732]
64. Akbari H, Macyszyn L, Da X, Bilello M, Wolf RL, et al. 2016 Imaging surrogates of infiltration obtained via multiparametric imaging pattern analysis predict subsequent location of recurrence of glioblastoma. Neurosurgery 78:572–80 [PubMed: 26813856]
65. Batmanghelich NK, Dalca A, Quon G, Sabuncu M, Golland P. 2016 Probabilistic modeling of imaging, genetics and diagnosis. IEEE Trans. Med. Imaging 35:1765–79 [PubMed: 26886973]
66. Rathore S, Akbari H, Doshi J, Shukla G, Rozycki M, et al. 2018 Radiomic signature of infiltration in peritumoral edema predicts subsequent recurrence in glioblastoma: implications for personalized radiotherapy planning. J. Med. Imaging 5:021219
67. Macyszyn L, Akbari H, Pisapia JM, Da X, Attiah M, et al. 2016 Imaging patterns predict patient survival and molecular subtype in glioblastoma via machine learning techniques. Neuro-Oncology 18:417–25 [PubMed: 26188015]
68. Rathore S, Akbari H, Rozycki M, Bakas S, Davatzikos C. 2016 Imaging pattern analysis reveals three distinct phenotypic subtypes of GBM with different survival rates. Neuro-Oncology 18:vi128
69. Rathore S, Akbari H, Nasrallah M, Bakas S, Binder Z, et al. 2018 Quantitative multi-parametric profiling reveals remarkable heterogeneity within IDH-wildtype glioblastoma, offering prognostic stratification beyond current WHO classifications. Neuro-Oncology 20:vi186
70. Rathore S, Akbari H, Rozycki M, Abdullah KG, Nasrallah MP, et al. 2018 Radiomic MRI signature reveals three distinct subtypes of glioblastoma with different clinical and molecular characteristics, offering prognostic value beyond IDH1. Sci. Rep 8:5087 [PubMed: 29572492]
71. Tarantola A 2005 Inverse Problem Theory and Methods for Model Parameter Estimation. Philadelphia: Soc. Ind. Appl. Math. (SIAM)
72. Benzekry S, Lamont C, Beheshti A, Tracz A, Ebos JML, et al. 2014 Classical mathematical models for description and prediction of experimental tumor growth. PLOS Comput. Biol 10:e1003800 [PubMed: 25167199]
73. Collis J, Connor A, Paczkowski M, Kannan P, Pitt-Francis J, et al. 2017 Bayesian calibration, validation, and uncertainty quantification for predictive modelling of tumour growth: a tutorial. Bull. Math. Biol 79:939–74 [PubMed: 28290010]
74. Hormuth DA II, Weis JA, Barnes SL, Miga MI, Rericha EC, et al. 2015 Predicting *in vivo* glioma growth with the reaction diffusion equation constrained by quantitative magnetic resonance imaging data. Phys. Biol 12:046006 [PubMed: 26040472]
75. Hormuth DA II, Weis JA, Barnes SL, Miga MI, Rechricha EC, et al. 2017 A mechanically coupled reaction-diffusion model that incorporates intratumoural heterogeneity to predict *in vivo* glioma growth. J. R. Soc. Interface 14:20161010 [PubMed: 28330985]
76. Oden JT, Hawkins A, Prudhomme S. 2010 General diffuse-interface theories and an approach to predictive tumor growth modeling. Math. Models Methods Appl. Sci 20:477–517
77. Wong KCL, Summers RM, Kebebew E, Yao J. 2015 Pancreatic tumor growth prediction with multiplicative growth and image-derived motion In Information Processing in Medical Imaging. IPMI 2015, ed. Ourselin S, Alexander D, Westin CF, Cardoso M, pp. 501–3. Cham, Switz.: Springer
78. Rahman MM, Feng Y, Yankeelov TE, Oden JT. 2017 A fully coupled space-time multiscale modeling framework for predicting tumor growth. Comput. Methods Appl. Mech. Eng 320:261–86 [PubMed: 29158608]
79. Rekik I, Allassonnière S, Clatz O, Geremia E, Stretton E, et al. 2013 Tumor growth parameters estimation and source localization from a unique time point: application to low-grade gliomas. Comput. Vis. Image Understanding 117:238–49
80. Baldock AL, Ahn S, Rockne R, Johnston S, Neal M, et al. 2014 Patient-specific metrics of invasiveness reveal significant prognostic benefit of resection in a predictable subset of gliomas. PLOS ONE 9:e99057 [PubMed: 25350742]
81. Mosayebi P, Cobzas D, Murtha A, Jagersand M. 2012 Tumor invasion margin on the Riemannian space of brain fibers. Med. Image Anal 16:361–73 [PubMed: 22154876]

82. Corwin D, Holdsworth C, Rockne RC, Trister AD, Mrugala MM, et al. 2013 Toward patient-specific biologically optimized radiation therapy plans for the treatment of glioblastoma. PLOS ONE 8:e79115 [PubMed: 24265748]
83. Lê M, Delingette H, Kalpathy-Cramer J, Gerstner ER, Batchelor T, et al. 2017 Personalized radiotherapy planning based on a computational tumor growth model. IEEE Trans. Med. Imaging 36:815–25 [PubMed: 28113925]
84. Unkelbach J, Menze BH, Konukoglu E, Dittmann F, Ayache N, Shih HA. 2014 Radiotherapy planning for glioblastoma based on a tumor growth model: implications for spatial dose redistribution. Phys. Med. Biol 59:771–89 [PubMed: 24440905]
85. Swanson KR, Rostomily RC, Alvord EC. 2008 A mathematical modelling tool for predicting survival of individual patients following resection of glioblastoma: a proof of principle. Br. J. Cancer 98:113–19 [PubMed: 18059395]
86. Wasserman RM, Acharya RS, Sibata C, Shin KH. 1996 Patient-specific tumor prognosis prediction via multimodality imaging. Proc. SPIE 2709:468–79
87. Jackson PR, Juliano J, Hawkins-Daarud A, Rockne RC, Swanson KR. 2015 Patient-specific mathematical neuro-oncology: using a simple proliferation and invasion tumor model to inform clinical practice. Bull. Math. Biol 77:846–56 [PubMed: 25795318]
88. Lima EABF, Oden JT, Wohlmuth B, Shahmoradi A, Hormuth DA, et al. 2017 Selection and validation of predictive models of radiation effects on tumor growth based on noninvasive imaging data. Comput. Methods Appl. Mech. Eng 327:227–308
89. Powathil G, Kohandel M, Sivaloganathan S, Oza A, Milosevic M. 2007 Mathematical modeling of brain tumors: effects of radiotherapy and chemotherapy. Phys. Med. Biol 52:3291–306 [PubMed: 17505103]
90. Weis JA, Miga MI, Yankeelov TE. 2017 Three-dimensional image-based mechanical modeling for predicting the response of breast cancer to neoadjuvant therapy. Comput. Methods Appl. Mech. Eng 314:494–512 [PubMed: 28042181]
91. Scheufele K, Mang A, Gholami A, Davatzikos C, Biros G, Mehl M. 2019 Coupling brain-tumor biophysical models and diffeomorphic image registration. Comput. Methods Appl. Mech. Eng 347:533–67 [PubMed: 31857736]
92. Zacharaki EI, Hogea CS, Shen D, Biros G, Davatzikos C. 2009 Non-diffeomorphic registration of brain tumor images by simulating tissue loss and tumor growth. NeuroImage 46:762–74 [PubMed: 19408350]
93. Stefanescu R, Commowick O, Maladain G, Bondiau PY, Ayache N, Pennec X. 2004 Non-rigid atlas to subject registration with pathologies for conformal brain radiotherapy In International Conference on Medical Image Computing and Computer-Assisted Intervention—MICCAI 2004, ed. Barillot C, Haynor DR, Hellier P, pp. 704–11. Lecture Notes in Computer Science, Vol. 3216 Berlin/Heidelberg: Springer
94. Angelini ED, Clatz O, Mandonnet E, Konukoglu E, Capelle L, Duffau H. 2007 Glioma dynamics and computational models: a review of segmentation, registration, in silico growth algorithms and their clinical applications. Curr. Med. Imaging Rev 3:262–76
95. Bauer S, Wiest R, Nolte LP, Reyes M. 2013 A survey of MRI-based medical image analysis for brain tumor studies. Phys. Med. Biol 58:R97–129 [PubMed: 23743802]
96. Bakas S, Zeng K, Sotiras A, Rathore S, Akbari H, et al. 2016 GLISTRboost: combining multimodal MRI segmentation, registration, and biophysical tumor growth modeling with gradient boosting machines for glioma segmentation. Brainlesion 9556:144–55 [PubMed: 28725877]
97. Mia H, Petitjean C, Vera P, Ruan S. 2015 Joint tumor growth prediction and tumor segmentation on therapeutic follow-up PET images. Med. Image Anal 23:84–91 [PubMed: 25988489]
98. Hogea C, Davatzikos C, Biros G. 2008 Brain-tumor interaction biophysical models for medical image registration. SIAM J. Imaging Sci 30:3050–72
99. Mang A, Toma A, Schuetz TA, Becker S, Buzug TM. 2012 A generic framework for modeling brain deformation as a constrained parameteric optimization problem to aid non-diffeomorphic image registration in brain tumor imaging. Methods Inform. Med 51:429–40
100. Bellomo N, Li NK, Maini PK. 2008 On the foundations of cancer modelling: selected topics, speculations, and perspectives. Math. Models Methods Appl. Sci 18:593–646

101. Roose T, Chapman SJ, Maini PK. 2007 Mathematical models of avascular tumor growth. SIAM Rev. 49:179–208
102. Wang Z, Deisboeck TS. 2008 Computational modeling of brain tumors: discrete, continuum or hybrid? Sci. Model. Simul 15:381–93
103. Harpold HLP, Alvord EC, Swanson KR. 2007 The evolution of mathematical modeling of glioma proliferation and invasion. J. Neuropathol. Exp. Neurol 66:1–9 [PubMed: 17204931]
104. Hawkins-Daarud A, Rockne RC, Anderson ARA, Swanson KR. 2013 Modeling tumor-associated edema in gliomas during anti-angiogenic therapy and its impact on imageable tumor. Front. Oncol 3:66 [PubMed: 23577324]
105. Gu S, Chakraborty G, Champley K, Alessio AM, Claridge J, et al. 2012 Applying a patient-specific biomathematical model of glioma growth to develop virtual [18F]-FMISO-PET images. Math. Med. Biol 29:31–48 [PubMed: 21562060]
106. Schuetz TA, Becker S, Mang A, Toma A, Buzug TM. 2013 Modelling of glioblastoma growth by linking a molecular interaction network with an agent based model. Math. Comput. Model. Dyn. Syst 19:417–33
107. Toma A, Mang A, Schuetz TA, Becker S, Buzug TM. 2012 A novel method for simulating the extracellular matrix in models of tumour growth. Comput. Math. Methods Med 2012:109019 [PubMed: 22919426]
108. Toma A, del Rocío Cisneros Castillo L, Schuetz TA, Becker S, Mang A, et al. 2013 A validated mathematical model of tumour-immune interactions for glioblastoma. Curr. Med. Imaging Rev 9:145–53
109. Swanson KR, Alvord EC, Murray JD. 2000 A quantitative model for differential motility of gliomas in grey and white matter. Cell Proliferation 33:317–30 [PubMed: 11063134]
110. Swanson KR, Alvord EC, Murray JD. 2002 Virtual brain tumours (gliomas) enhance the reality of medical imaging and highlight inadequacies of current therapy. Br. J. Cancer 86:14–18 [PubMed: 11857005]
111. Swanson KR, Bridge C, Murray JD, Alvord EC. 2003 Virtual and real brain tumors: using mathematical modeling to quantify glioma growth and invasion. J. Neurol. Sci 216:1–10 [PubMed: 14607296]
112. Deisboeck TS, Wang Z, Macklin P, Cristini V. 2011 Multiscale cancer modeling. Annu. Rev. Biomed. Eng 13:127–55 [PubMed: 21529163]
113. Lowengrub JS, Frieboes HB, Jin F, Chuang YL, Li X, et al. 2009 Nonlinear modelling of cancer: bridging the gap between cells and tumours. Nonlinearity 23:R1–R91
114. Schuetz TA, Mang A, Becker S, Toma A, Buzug TM. 2014 Identification of crucial parameters in a mathematical multiscale model of glioblastoma growth. Comput. Math. Methods Med 2014:437094 [PubMed: 24899919]
115. Mang A 2014 Methoden zur Numerischen Simulation der Progression von Gliomen: Modellentwicklung, Numerik und Parameteridentifikation. Wiesbaden, Ger.: Springer Fachmedien
116. Gholami A, Mang A, Biros G. 2016 An inverse problem formulation for parameter estimation of a reaction-diffusion model of low grade gliomas. J. Math. Biol 72:409–33 [PubMed: 25963601]
117. Jbabdi S, Mandonnet E, Duffau H, Capelle L, Swanson KR, et al. 2005 Simulation of anisotropic growth of low-grade gliomas using diffusion tensor imaging. Magn. Reson. Med 54:616–24 [PubMed: 16088879]
118. Mang A, Toma A, Schuetz TA, Becker S, Eckey T, et al. 2012 Biophysical modeling of brain tumor progression: from unconditionally stable explicit time integration to an inverse problem with parabolic PDE constraints for model calibration. Med. Phys 39:4444–59 [PubMed: 22830777]
119. Konukoglu E, Clatz O, Menze BH, Stieltjes B, Weber MA, et al. 2010 Image guided personalization of reaction-diffusion type tumor growth models using modified anisotropic eikonal equations. IEEE Trans. Med. Imaging 29:77–95 [PubMed: 19605320]
120. Mohamed A, Davatzikos C. 2005 Finite element modeling of brain tumor mass-effect from 3D medical images In Medical Image Computing and Computer-Assisted Intervention—MICCAI 2005, ed. Duncan JS, Gerig G, pp. 400–8. Berlin/Heidelberg: Springer

121. Hogea C, Davatzikos C, Biros G. 2007 Modeling glioma growth and mass effect in 3D MR images of the brain In Medical Image Computing and Computer-Assisted Intervention—MICCAI 2007, ed. Ayache N, Ourselin S, Maeder A, pp. 642–50. Lecture Notes in Computer Science, Vol. 4791 Berlin/Heidelberg: Springer
122. Subramanian S, Gholami A, Biros G. 2019 Simulation of glioblastoma growth using a 3D multispecies tumor model with mass effect. J. Math. Biol 79:941–67 [PubMed: 31127329]
123. Hatzikirou H, Basanta D, Simon M, Schaller K, Deutsch A. 2012 Go or grow: the key to the emergence of invasion in tumour progression? Math. Med. Biol 29:49–65 [PubMed: 20610469]
124. Swanson KR, Rockne RC, Claridge J, Chaplain MA, Alvord EC, Anderson AR. 2011 Quantifying the role of angiogenesis in malignant progression of gliomas: in silico modeling integrates imaging and histology. Cancer Res. 71:7366–75 [PubMed: 21900399]
125. Saut O, Lagaert JB, Colin T, Fathallah-Shaykh HM. 2014 A multilayer grow-or-go model for GBM: effects of invasive cells and anti-angiogenesis on growth. Bull. Math. Biol 76:2306–33 [PubMed: 25149139]
126. Goriely A, Geers MGD, Holzapfel GA, Jayamohan J, Jérusalem A, et al. 2015 Mechanics of the brain: perspectives, challenges, and opportunities. Biomech. Model. Mechanobiol 14(5):931–65 [PubMed: 25716305]
127. Ambrosi D, Ateshian GA, Arruda EM, Cowin SC, Dumais J, et al. 2011 Perspectives on biological growth and remodeling. J. Mech. Phys. Solids 59(4):863–83 [PubMed: 21532929]
128. Rutter EM, Stepien TL, Anderies BJ, Plasencia JD, Woolf EC, et al. 2017 Mathematical analysis of glioma growth in a murine model. Sci. Rep 7:2508 [PubMed: 28566701]
129. Liu Y, Sadowki SM, Weisbrod AB, Kebebew E, Summers RM, Yao J. 2014 Patient specific tumor growth prediction using multimodal images. Med. Image Anal 18:555–66 [PubMed: 24607911]
130. Lê M, Delingette H, Kalpathy-Cramer J, Gerstner ER, Batchelor T, et al. 2015 Bayesian personalization of brain tumor growth model In Medical Image Computing and Computer-Assisted Intervention—MICCAI 2015, ed. Navab N, Hornegger J, Wells W, Frangi A, pp. 424–32. Lecture Notes in Computer Science, Vol 9350 Cham, Switz.: Springer
131. Knopoff D, Fernández DR, Torres GA, Turner CV. 2017 A mathematical method for parameter estimation in a tumor growth model. Comput. Appl. Math 36:733–48
132. Colin T, Iollo A, Lagaert JB, Saut O. 2014 An inverse problem for the recovery of the vascularization of a tumor. J. Inverse Ill-Posed Probl 22:759–86
133. Feng X, Hormuth DA, Yankeelov TE. 2018 An adjoint-based method for a linear mechanically-coupled tumor model: application to estimate the spatial variation of murine glioma growth based on diffusion weighted magnetic resonance imaging. Comput. Mech 63:159–80 [PubMed: 30880856]
134. Knopoff DA, Fernández DR, Torres GA, Turner CV. 2013 Adjoint method for a tumor growth PDE-constrained optimization problem. Comput. Math. Appl 66:1104–19
135. Quiroga AAI, Fernández D, Torres GA, Turner CV. 2015 Adjoint method for a tumor invasion PDE-constrained optimization problem in 2D using adaptive finite element method. Appl. Math. Comput 270:358–68
136. Gholami A, Mang A, Scheufele K, Davatzikos C, Mehl M, Biros G. 2017 A framework for scalable biophysics-based image analysis In SC ‘17: Proceedings of the International Conference for High Performance Computing, Networking, Storage and Analysis, Art. No. 19. New York: Assoc. Comput. Mach.
137. Subramanian S, Scheufele K, Mehl M, Biros G. 2019 Where did the tumor start? An inverse solver with sparse localization for tumor growth models. arXiv:1907.06564 [physics.med-ph]
138. Jaroudi R, Baravdish G, Johansson BT, Aström F. 2019 Numerical reconstruction of brain tumours. Inverse Probl. Sci. Eng 27:278–98
139. Hawkins-Daarud A, Prudhomme S, van der Zee KG, Oden JT. 2013 Bayesian calibration, validation, and uncertainty quantification of diffuse interface models of tumor growth. J. Math. Biol 67:1457–85 [PubMed: 23053536]
140. Menze BH, Van Leemput K, Honkela A, Konukoglu E, Weber MA, et al. 2011 A generative approach for image-based modeling of tumor growth In Information Processing in Medical Imaging. IPMI 2011, ed. Székely G, Hahn HK, pp. 735–47. Berlin/Heidelberg: Springer

141. Oden JT, Prudencio EE, Hawkins-Daarud A. 2013 Selection and assessment of phenomenological models of tumor growth. Math. Models Methods Appl. Sci 23:1309–38
142. Paek J, Choi I. 2014 Bayesian inference of the stochastic Gompertz growth model of tumor growth. Commun. Stat. Appl. Methods 21:521–28
143. Meghdadi N, Niroomand-Oscuii H, Soltani M, Ghalichi F, Pourgolmohammad M. 2017 Brain tumor growth simulation: model validation and uncertainty quantification. Int. J. Syst. Assur. Eng 8:655–62
144. Kahle C, Lam KF. 2018 Parameter identification via optimal control for a Cahn-Hilliard-chemotaxis system with a variable mobility. Appl. Math. Optim 10.1007/s00245-018-9491-z
145. Patmanidis S, Charalampidis AC, Kordonis I, Mitsis GD, Papavassilopoulos GP. 2018 Tumor growth modeling: parameter estimation with maximum likelihood methods. Comput. Methods Programs Biomed 160:1–10 [PubMed: 29728236]
146. Kahle C, Lam KF, Latz J, Ullmann E. 2019 Bayesian parameter identification in Cahn-Hilliard models for biological growth. SIAM/ASA J. Uncertain. Quantif 7(2):526–52
147. Prastawa M, Buillitt E, Gerig G. 2009 Simulation of brain tumors in MR images for evaluation of segmentation efficacy. Med. Image Anal 13:297–311 [PubMed: 19119055]
148. Mohamed A, Shen D, Davatzikos C. 2006 Deformable registration of brain tumor images via a statistical model of tumor-induced deformation. Med. Image Anal 10:752–63 [PubMed: 16860588]
149. Kwon D, Niethammer M, Akbari H, Bilello M, Davatzikos C, Pohl KM. 2014 PORTR: pre-operative and post-recurrence brain tumor registration. IEEE Trans. Med. Imaging 33:651–67 [PubMed: 24595340]
150. Deeley MA, Chen A, Datteri R, Noble JH, Cmelak AJ, et al. 2011 Comparison of manual and automatic segmentation methods for brain structures in the presence of space-occupying lesions: a multi-expert study. Phys. Med. Biol 56:4557–77 [PubMed: 21725140]
151. Mazzara GP, Velthuizen RP, Pearlman JL, Greenberg HM, Wagner H. 2004 Brain tumor target volume determination for radiation treatment planning through automated MRI segmentations. Int. J. Radiat. Oncol. Biol. Phys 59:300–12 [PubMed: 15093927]
152. Isin A, Direkoglu C, Sah M. 2016 Review of MRI-based brain tumor image segmentation using deep learning methods. Procedia Comput. Sci 102:317–24
153. Gholami A, Subramanian S, Shenoy V, Himthani N, Yue X, et al. 2019 A novel domain adaptation framework for medical image segmentation In Brainlesion: Glioma, Multiple Sclerosis, Stroke and Traumatic Brain Injuries. BrainLes 2018, ed. Crimi A, Bakas S, Kuijf H, Keyvan F, Reyes M, Walsum T van, pp. 289–98. Lecture Notes in Computer Science, Vol. 11384 Cham, Switz.: Springer
154. Sotiras A, Davatzikos C, Paragios N. 2013 Deformable medical image registration: a survey. IEEE Trans. Med. Imaging 32:1153–90 [PubMed: 23739795]
155. Mang A, Schnabel JA, Crum WR, Modat M, Camara-Rey O, et al. 2008 Consistency of parametric registration in serial MRI studies of brain tumor progression. Int. J. Comput. Assisted Radiol. Surg 3:201–11
156. Mang A, Crum WR, Camara-Rey O, Schnabel JA, Penney GP, et al. 2007 Modelling tumour growth patterns with non-rigid image registration In Advances in Medical Engineering, ed. Buzug TM, Holz D, Bongartz J, Kohl-Bareis M, Hartmann U, Weber S, pp. 139–44. Springer Proceedings in Physics, Vol. 114 Berlin/Heidelberg: Springer
157. Han X, Bakas S, Kwitt R, Aylward S, Akbari H, et al. 2019 Patient-specific registration of pre-operative and post-recurrence brain tumor MRI scans In Brainlesion: Glioma, Multiple Sclerosis, Stroke and Traumatic Brain Injuries. BrainLes 2018, ed. Crimi A, Bakas S, Kuijf H, Keyvan F, Reyes M, Walsum T van, pp. 105–14. Lecture Notes in Computer Science, Vol. 11383 Cham, Switz.: Springer
158. Bilello M, Akbari H, Da X, Pisapia JM, Mohan S, et al. 2016 Population-based MRI atlases of spatial distribution are specific to patient and tumor characteristics in glioblastoma. NeuroImage Clin. 12:34–40 [PubMed: 27358767]
159. Zacharaki EI, Hogea CS, Shen D, Biros G, Davatzikos C. 2008 Parallel optimization of tumor model parameters for fast registration of brain tumor images. Proc. SPIE 6914:69140K

160. Henn S, Hömke L, Witsch K. 2004 Lesion preserving image In Pattern Recognition. DAGM 2004, ed. Rasmussen CE, Bülthof HH, Schölkopf B, Giese MA, pp. 496–503. Lecture Notes in Computer Science, Vol. 3175 Berlin/Heidelberg: Springer

161. Brett M, Leff AP, Rorden C, Ashburner J. 2001 Spatial normalization of brain images with focal lesions using cost function masking. NeuroImage 14:486–500 [PubMed: 11467921]

162. Parisot S, Wells W, Chemouny S, Duffau H, Paragios N. 2014 Concurrent tumor segmentation and registration with uncertainty-based sparse non-uniform graphs. Med. Image Anal 18:647–59 [PubMed: 24717540]

163. Li X, Long X, Laurienti P, Wyatt C. 2012 Registration of images with varying topology using embedded maps. IEEE Trans. Med. Imaging 31:749–65 [PubMed: 22194239]

164. Scheufele K, Subramanian S, Mang A, Biros G, Mehl M. 2019 Image-driven biophysical tumor growth model calibration. arXiv:1907.07774 [q-bio.QM]

165. Zacharaki EI, Hogea CS, Biros G, Davatzikos C. 2008 A comparative study of biomechanical simulators in deformable registration of brain tumor images. IEEE Trans. Biomed. Eng 55:1233–36 [PubMed: 18334420]

166. Mang A, Tharakan S, Gholami A, Nimthani N, Subramanian S, et al. 2017 SIBIA-GlS: scalable biophysics-based image analysis for glioma segmentation. In Proceedings of the 6th MICCAI BraTS Challenge, pp. 197–204. https://www.cbica.upenn.edu/sbia/Spyridon.Bakas/MICCAI_BraTS/MICCAI_BraTS_2017_proceedings_shortPapers.pdf

167. Gooya A, Pohl KM, Bilello M, Biros G, Davatzikos C. 2011 Joint segmentation and deformable registration of brain scans guided by a tumor growth model In Medical Image Computing and Computer-Assisted Intervention—MICCAI 2011, ed. Fichtinger G, Martel A, Peters T, pp. 532–40. Lecture Notes in Computer Science, Vol. 6892 Berlin/Heidelberg: Springer

168. Hogea C, Davatzikos C, Biros G. 2008 An image-driven parameter estimation problem for a reaction-diffusion glioma growth model with mass effects. J. Math. Biol 56:793–825 [PubMed: 18026731]

169. Friedman JH. 2001 Greedy function approximation: a gradient boosting machine. Ann. Stat 29:1189–232

170. Friedman JH. 2002 Stochastic gradient boosting. Comput. Stat. Data Anal 38:367–78

171. Gaonkar B, Macyszyn L, Bilello M, Sadaghiani MS, Akbari H, et al. 2015 Automated tumor volumetry using computer-aided image segmentation. Acad. Radiol 22:653–61 [PubMed: 25770633]

172. Bakas S, Chatzimichail K, Hunter G, Labbé B, Sidhu PS, et al. 2017 Fast semi-automatic segmentation of focal liver lesions in contrast-enhanced ultrasound, based on a probabilistic model. Comput. Methods Biomech. Biomed. Eng. Imaging Vis 5:329–38

173. Mang A, Biros G. 2015 An inexact Newton–Krylov algorithm for constrained diffeomorphic image registration. SIAM J. Imaging Sci 8:1030–69 [PubMed: 27617052]

174. Mang A, Gholami A, Biros G. 2016 Distributed-memory large-deformation diffeomorphic 3D image registration. In SC'16: Proceedings of the International Conference for High Performance Computing, Networking, Storage and Analysis, Salt Lake City, UT, 2016, pp. 842–53. https://ieeexplore.ieee.org/document/7877150

175. Mang A, Gholami A, Davatzikos C, Biros G. 2019 CLAIRE: a distributed-memory solver for constrained large deformation diffeomorphic image registration. SIAM J. Sci. Comput 41(5):C548–C584

176. Davatzikos C, Sotiras A, Fan Y, Habes M, Erus G, et al. 2019 Precision diagnostics based on machine learning-derived imaging signatures. Magn. Reson. Imaging 64:49–61 [PubMed: 31071473]

177. Tracqui P 2009 Biophysical models of tumour growth. Rep. Progress Phys 72:056701

178. Shukla G, Alexander GS, Bakas S, Nikam R, Talekar K, et al. 2017 Advanced magnetic resonance imaging in glioblastoma: a review. Chinese Clin. Oncol 6:40

179. Zeng K, Bakas S, Sotiras A, Akbari H, Rozycki M, et al. 2016 Segmentation of gliomas in pre-operative and post-operative multimodal magnetic resonance imaging volumes based on a hybrid generative-discriminative framework In Brainlesion: Glioma, Multiple Sclerosis, Stroke and

Traumatic Brain Injuries. BrainLes 2016, ed. Crimi A, Menze B, Maier C, Reyes M, Winzeck S, Handels H, pp. 184–94. Lecture Notes in Computer Science, Vol. 10154 Cham, Switz.: Springer

180. Kwon D, Shinohara RT, Akbari H, Davatzikos C. 2014 Combining generative models for multifocal glioma segmentation and registration. Med. Image Comput. Comput. Assist. Interv 17(Pt. 1):763–70 [PubMed: 25333188]
181. Kwon D, Akbari H, Da X, Gaonkar B, Davatzikos C. 2014 Multimodal brain tumor image segmentation using GLISTR. In Brain Tumor Segmentation (BraTS) Challenge Manuscripts, MICCAI 2014, pp. 18–19. http://people.csail.mit.edu/menze/papers/proceedings_miccai_brats_2014.pdf
182. Davatzikos C, Rathore S, Bakas S, Pati S, Bergman M, et al. 2018 Cancer imaging phenomics toolkit: quantitative imaging analytics for precision diagnostics and predictive modeling of clinical outcome. J. Med. Imaging 5:011018
183. Rathore S, Bakas S, Pati S, Akbari H, Kalarot R, et al. 2018 Brain cancer imaging phenomics toolkit (brain-CaPTk): an interactive platform for quantitative analysis of glioblastoma In Brainlesion: Glioma, Multiple Sclerosis, Stroke and Traumatic Brain Injuries. BrainLes 2017, ed. Crimi A, Bakas S, Kuijf H, Menze B, Reyes M, pp. 133–45. Lecture Notes in Computer Science, Vol. 10670 Cham, Switz.: Springer
184. Wang CH, Rockhill JK, Mrugala M, Peacock DL, Lai A, et al. 2009 Prognostic significance of growth kinetics in newly diagnosed glioblastomas revealed by combining serial imaging with a novel biomathematical model. Cancer Res. 69:9133–40 [PubMed: 19934335]
185. Rathore S, Bakas S, Akbari H, Shukla G, Rozycki M, Davatzikos C. 2018 Deriving stable multi-parametric MRI radiomic signatures in the presence of inter-scanner variations: survival prediction of glioblastoma via imaging pattern analysis and machine learning techniques. Proc. SPIE 10575:1057509
186. Rathore S, Bakas S, Akbari H, Rozycki M, Davatzikos C. 2018 Quantitative imaging predictors of overall survival in glioblastoma patients robust in the presence of inter-scanner variations. Neuro-Oncology 20:vi184
187. Shukla G, Bakas S, Rathore S, Akbari H, Sotiras A, Davatzikos C. 2017 Radiomic features from multi-institutional glioblastoma MRI offer additive prognostic value to clinical and genomic markers: focus on TCGA-GBM collection. Int. J. Radiat. Oncol. Biol. Phys 99:E107–E108
188. Petrecca K, Guiot MC, Panet-Raymond V, Souhami L. 2013 Failure pattern following complete resection plus radiotherapy and temozolomide is at the resection margin in patients with glioblastoma. J. Neuro-Oncol 111:19–23
189. Lemée JM, Clavreul A, Menei P. 2015 Intratumoral heterogeneity in glioblastoma: Don't forget the peritumoral brain zone. Neuro-Oncology 17:1322–32 [PubMed: 26203067]
190. Chang EL, Akyurek S, Avalos T, Rebueno N, Spicer C, et al. 2007 Evaluation of peritumoral edema in the delineation of radiotherapy clinical target volumes for glioblastoma. Int. J. Radiat. Oncol. Biol. Phys 68:144–50 [PubMed: 17306935]
191. Bullitt E, Zeng D, Gerig G, Aylward S, Joshi S, et al. 2005 Vessel tortuosity and brain tumor malignancy: a blinded study. Acad. Radiol 12:1232–40 [PubMed: 16179200]
192. Kerbel RS. 2000 Tumor angiogenesis: past, present and the near future. Carcinogenesis 21:505–15 [PubMed: 10688871]
193. Ellingson BM, LaViolette PS, Rand SD, Malkin MG, Connelly JM, et al. 2011 Spatially quantifying microscopic tumor invasion and proliferation using a voxel-wise solution to a glioma growth model and serial diffusion MRI. Magn. Reson. Med 65:1131–43 [PubMed: 21413079]
194. Stein AM, Demuth T, Mobley D, Berens M, Sander LM. 2007 A mathematical model of glioblastoma tumor spheroid invasion in a three-dimensional in vitro experiment. Biophys. J 92:356–65 [PubMed: 17040992]
195. Burgess PK, Kulesa PM, Murray JD, Alvord EC Jr. 1997 The interaction of growth rates and diffusion coefficients in a three-dimensional mathematical model of gliomas. J. Neuropathol. Exp. Neurol 56:704–13 [PubMed: 9184661]
196. Verhaak RG, Hoadley KA, Purdom E, Wang V, Qi Y, et al. 2010 Integrated genomic analysis identifies clinically relevant subtypes of glioblastoma characterized by abnormalities in PGFRA, IDH1, EGFR, and NF1. Cancer Cell 17:98–110 [PubMed: 20129251]

197. Sheller MJ, Reina GA, Edwards B, Martin J, Bakas S. 2018 Multi-institutional deep learning modeling without sharing patient data: a feasibility study on brain tumor segmentation In Brainlesion: Glioma, Multiple Sclerosis, Stroke and Traumatic Brain Injuries. BrainLes 2018, ed. Crimi A, Bakas S, Kuijf H, Keyvan F, Reyes M, Walsum T van, pp. 92–104. Lecture Notes in Computer Science, Vol. 11383 Cham, Switz.: Springer

198. Chang K, Balachandar N, Lam C, Yi D, Brown J, et al. 2018 Distributed deep learning networks among institutions for medical imaging. J. Am. Med. Inform. Assoc 25:945–54 [PubMed: 29617797]

## SHORTCOMINGS OF BIOPSIES

A biopsy (*a*) is localized and cannot capture the spatially heterogeneous molecular landscape (sampling error); (*b*) is typically not performed longitudinally (i.e., during and after treatment) due to its invasive nature and the potential of neurological deficit (monitoring limitation); (*c*) is not feasible for inaccessible, inoperable, and deep-seated tumors (anatomical constraints); and (*d*) might be unavailable in many clinical settings due to cost and equipment availability (economic challenge). Despite these shortcomings, tissue analysis provides ground truth and direct cancer molecular information.

## CHALLENGES FOR INTEGRATION OF MATHEMATICAL MODELS WITH IMAGING

- Tumor dynamics remain mostly unknown; tumor growth is a complex multiscale process that is not entirely understood and is challenging to capture mathematically. Tumor dynamics vary significantly across patients, and across space and time in a single patient due to differences in the local microenvironment and molecular alterations.
- It is not possible to conduct controlled experiments that allow for model refinement in humans. Animal models and in vitro cultures can help probe different mechanisms, but the genome, time scale, and overall environment are quite different in humans. As a result, assessment and validation remain challenging. This issue is further complicated by therapeutic intervention and resection, which are extremely hard to integrate or account for in a simulation-based framework.
- Mathematical models are typically parameterized by many unknown parameters. Calibrating such models requires patient-specific clinical data that are, in general, not available. For example, for GBM patients, most information regarding a tumor's state must be inferred from a single set of mpMRI scans (treatment is typically administered immediately after diagnosis).
- Even if the data were available, the ability to estimate unknown parameters is limited due to fundamental mathematical issues (e.g., nonconvexity and ill-posedness of the inverse problem; modeling the observation operator; selecting an appropriate regularization; differentiation and implementation of adjoint equations; noise and uncertainties in the data and model; modeling errors).
- The inverse problem poses computational challenges. If complex models are implemented naively, run times for calibrating them are prohibitive for clinical use. Indeed, even if the forward problem is linear, the inverse problem can be highly nonlinear. As a result, a single calibration can require hundreds of forward problem evaluations. If we consider uncertainty, the costs become even higher.

## CHALLENGES AND OPEN QUESTIONS IN BIOPHYSICAL INVERSION

Inverse problems pose not only computational challenges but also additional modeling challenges that have not been addressed thoroughly in existing work. Key questions are: (*a*) What is an appropriate mismatch function to quantify the discrepancy between model prediction and imaging data? (*b*) What are appropriate regularization models for $\boldsymbol{p}$? (*c*) How do numerical schemes affect the computed solutions? (*d*) How can we efficiently deal with the ill-posedness of the inverse problem? (*e*) How can we deal with sparse/scarce data? Although general frameworks from other disciplines do exist, specializing these techniques to the specific problem is critical for the clinical success of inverse modeling. Developing adequate methods for inverse modeling remains an open problem for biophysical models of tumor growth.

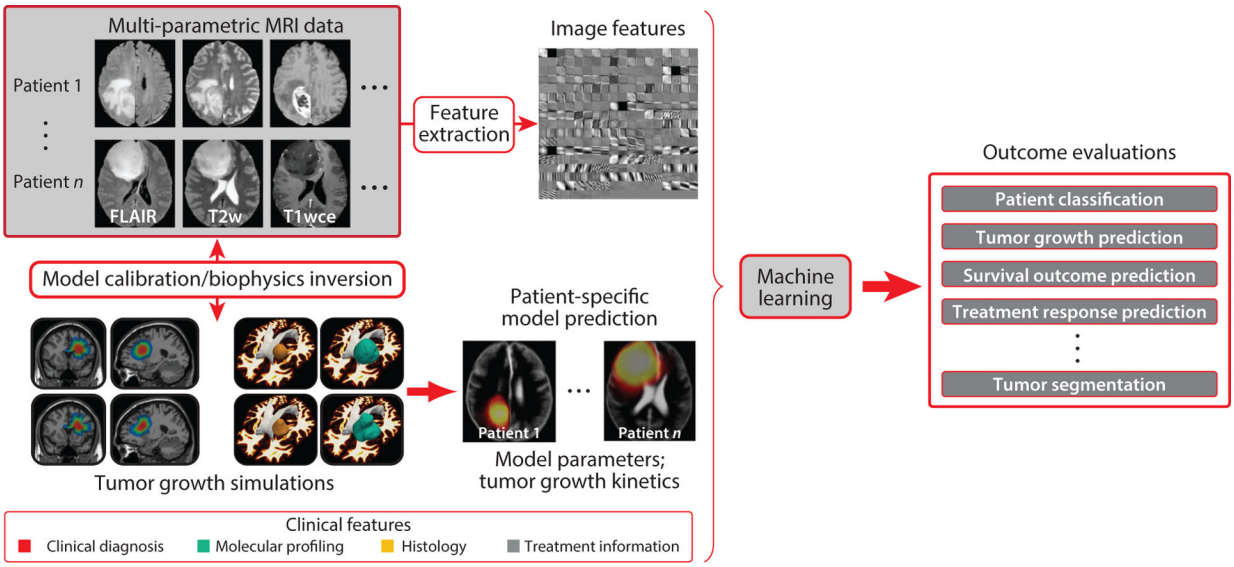


**Figure 1.**

Radiomics in neuro-oncology. We seek to extract quantitative imaging indicators that predict clinical outcome. The main inputs to our framework are multi-parametric magnetic resonance imaging (mpMRI) data (*top left*) and (possibly) clinical features such as molecular profiling and/or histopathological data (*bottom left*). One possible way to identify clinical markers in imaging data is to apply feature extraction methods from image analysis (*top center*). These methods do not, in general, incorporate any prior knowledge about the underlying pathology. Computer simulations of biophysical models can establish such a powerful tool to integrate such information. To be clinically useful, biophysical models must be calibrated using the mpMRI information (medical images in our case; *bottom left*). Once calibrated, these models can be used to generate patient-specific simulations (*bottom center*). In a final step, these quantitative parameters are integrated with machine learning algorithms to generate tools that can assist clinical decision making (*right block*). Images modified from Reference 3 with permission from Springer Nature, *Optimization and Engineering*, copyright 2018 Springer, and from Reference 4 with permission from IEEE, *IEEE Transactions on Medical Imaging*, copyright 2012 IEEE.

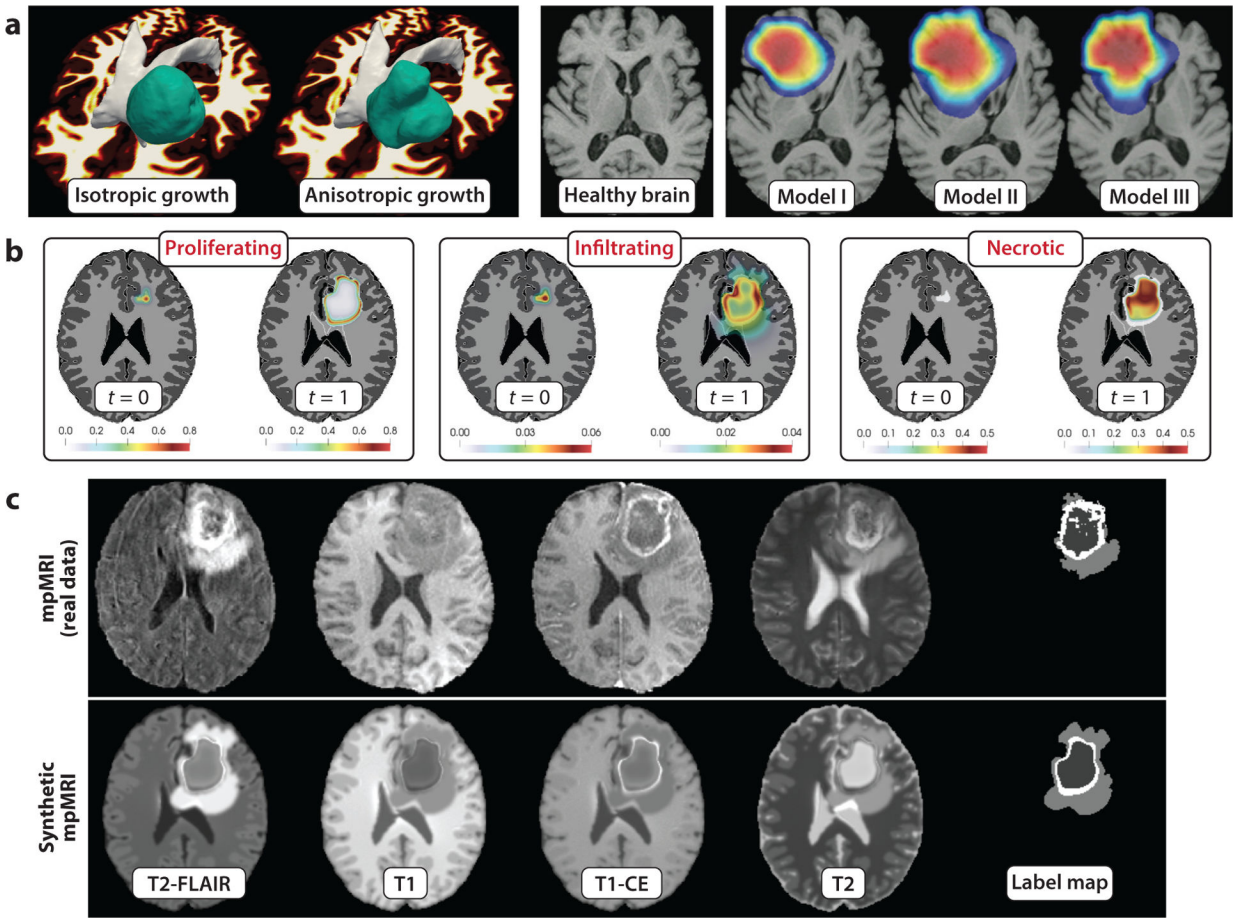


**Figure 2.**

Qualitative simulation results for different biophysical models. (*a*) Two single-species models, one without (*left*) and one with (*right*) mass effect. The three images on the right show results (axial slices through the brain) for different realizations of a mass effect model; we show different degrees of deformation of the healthy tissue due to tumor growth (98). (*b*) Simulation results for a multispecies model of tumor growth with mass effect (122). We show two time points (initial condition and final time) per tumor species (left to right: proliferating, infiltrating, and necrotic tumor cells). (*c*) This multispecies model allows us to account for imaging abnormalities seen in multi-parametric magnetic resonance imaging (mpMRI): (*top row*) patient-specific mpMRI data for a glioblastoma and (*bottom row*) synthetically generated mpMRI dataset using the model described in Reference 122. The model parameters were identified by manual trial and error; no inversion was performed. This figure has been modified from References 3, 98, and 122. Panel *a* (left) reprinted by permission from Springer Nature, *Optimization and Engineering*, copyright 2018 Springer. Panel *a* (right) reprinted by permission from the Society for Industrial and Applied Mathematics; copyright 2008, all rights reserved. Panels *b* and *c* reprinted by permission from Springer Nature, *Journal of Mathematical Biology*, copyright 2019 Springer.

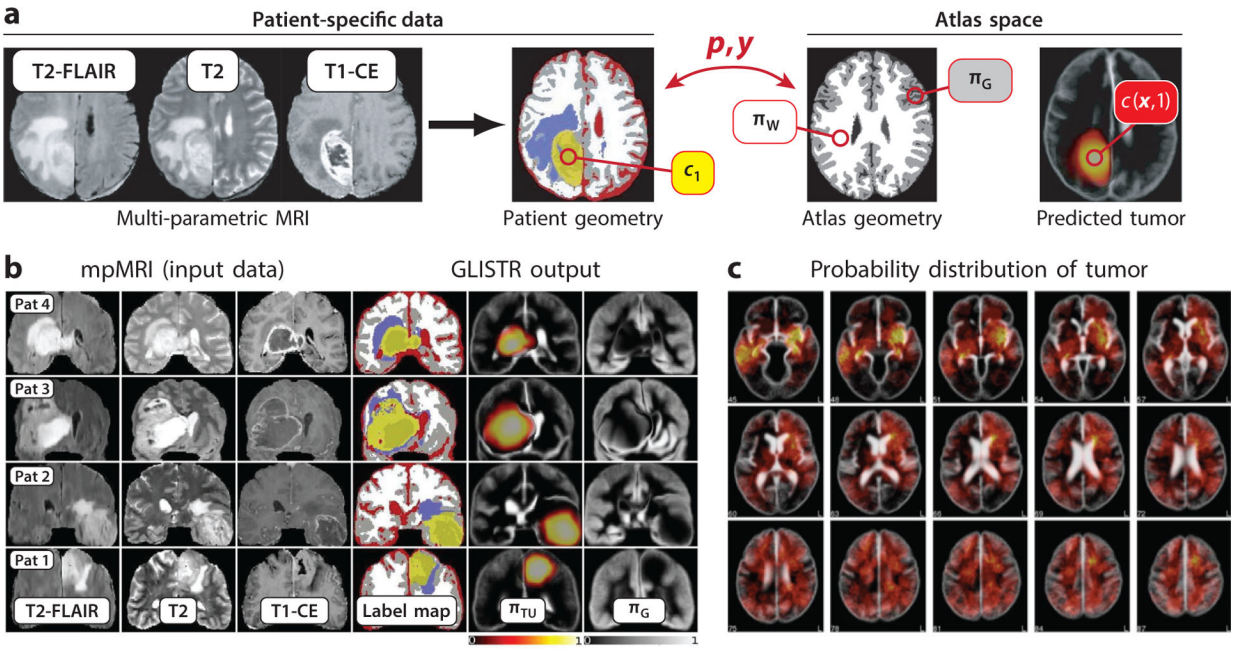


**Figure 3.**

(*a*) Illustration of the inverse problem of estimating patient-specific model parameters ***p***. We seek parameters ***p*** such that the predicted state $c(\boldsymbol{x}, 1)$ (solution of the forward problem) matches some observed data $c_{\text{OBS}}$. The input data to our problem are multi-parametric magnetic resonance imaging (mpMRI) data, shown at left. The image labeled "patient geometry" illustrates data we present to our solver. The image on the right shows the model output for the computed parameters. The simulations are performed in a tumor-free atlas image labeled "atlas geometry." To compensate for anatomical differences in patient and atlas geometry, we additionally invert for a deformation map ***y***. (*b*, *c*) Exemplary results for Glioma Image Segmentation and Registration (GLISTR) (4). We show segmentation results (*b*, coronal planes) and tumor probability maps (*c*, axial planes). (*b*) Each row corresponds to a different patient (bottom to top: patient 1 through patient 4). mpMRI (input data): The first three columns in panel *b* show the mpMRI data (input to our problem). The last three columns show the computed tumor labels $\xi$ [enhancing tumor region (ET), light yellow; necrotic and nonenhancing tumor region (NE), dark yellow; edematous/tumor-infiltrated tissue (ED), purple; cerebrospinal fluid (CSF), red; gray matter (GM), gray; white matter (WM), white], the probability map for the tumor $\boldsymbol{\pi}_{\text{TU}}$, and the probability map of GM $\boldsymbol{\pi}_{\text{G}}$. (*c*) The average of the computed tumor posteriors over 122 glioma cases. The color map is the same as the one used for $\boldsymbol{\pi}_{\text{TU}}$. It can be seen that within the considered patient population, the region with the highest tumor probability is placed in the left temporal lobe of the brain. Other abbreviations: CE, contrast-enhanced; FLAIR, fluid-attenuated inversion recovery. Figure modified from References 3 and 4. Panel *a* reprinted by permission from Springer Nature, *Optimization and Engineering*, copyright 2018 Springer. Panels *b* and *c* reprinted by permission from IEEE, *IEEE Transactions on Medical Imaging*, copyright 2012 IEEE.

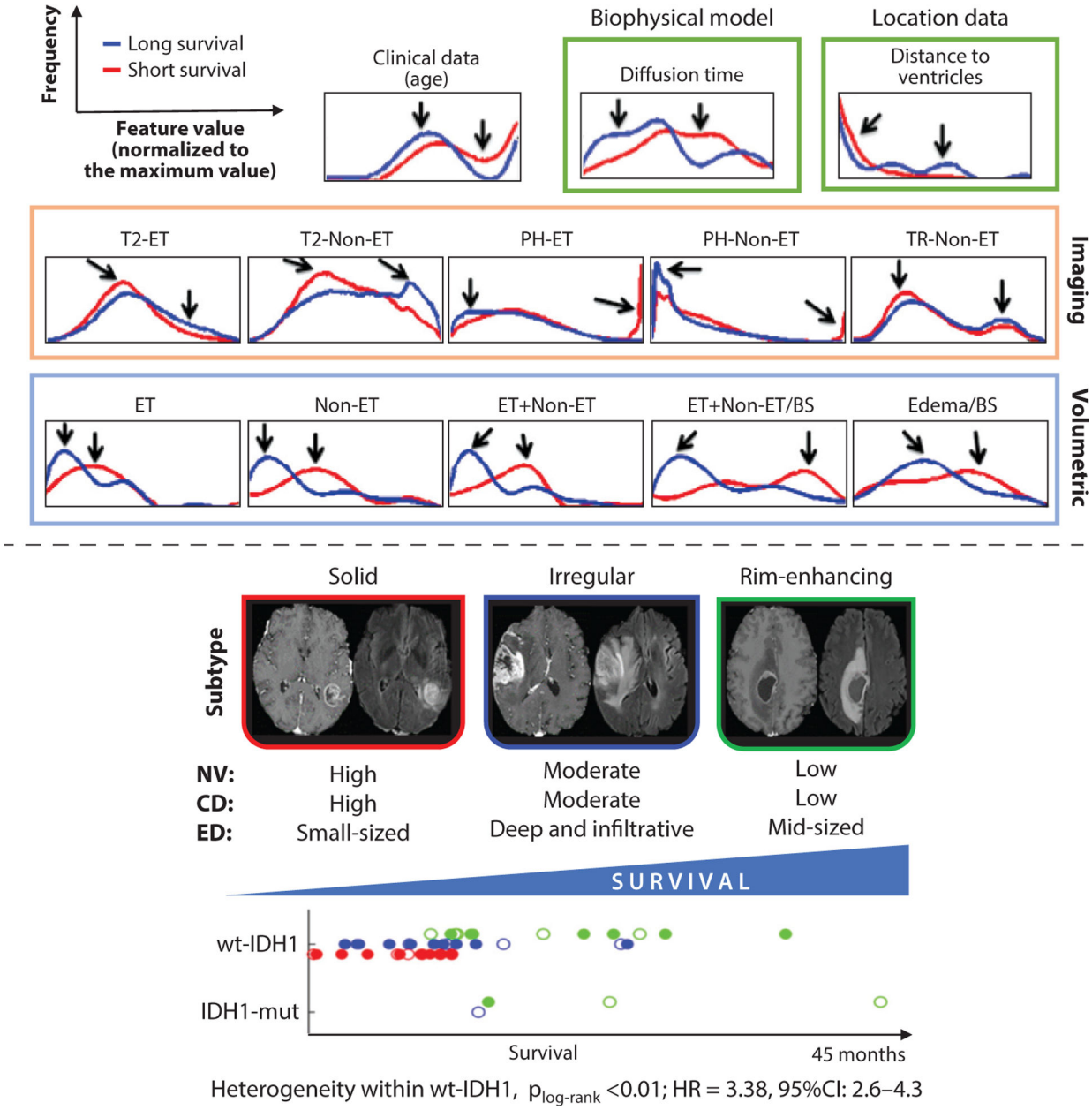


**Figure 4.**

Example studies on predicting patient overall survival (OS). (*Top*) Distributions of features most predictive of OS across long-survivor (*blue*) and short-survivor (*red*) groups. The black arrows point to larger differences between the groups, per feature. The diffusion time obtained via biophysical models of tumor growth is one of the most distinctive features. Panel modified with permission from Reference 67. (*Bottom*) Distinction of radiographic subtypes in relation to patient OS. The shortest survival of the isocitrate dehydrogenase-1 mutant (IDH1-mut) occurred in the irregular subtype, which overall had lower OS, indicating that the radiographic subtype can potentially add predictive value within IDH1-mut patients. Panel modified with permission from Reference 70. Abbreviations: BS, brain size; CD, cell density; ED, edematous/tumor-infiltrated tissue; ET, enhancing tumor; non-

ET, nonenhancing core of tumor; NV, neovascularization; PH, peak height of perfusion signal; TR, trace.

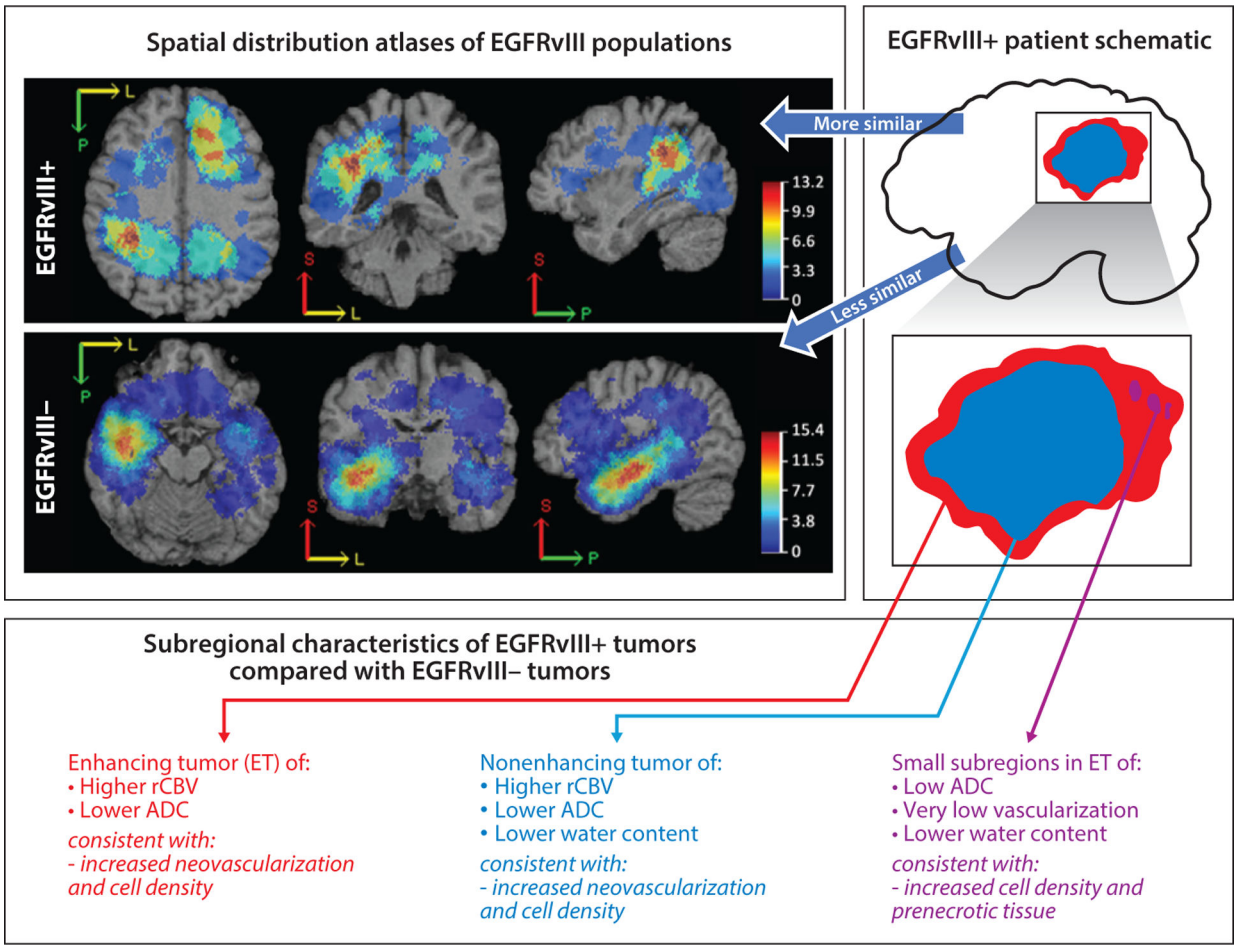


**Figure 5.**

Spatial descriptive characteristics of EGFRvIII glioblastoma, following advanced computational analysis incorporating biophysical tumor growth modeling. Abbreviations: ADC, apparent diffusion coefficient; ET, enhancing tumor; rCBV, relative cerebral blood volume. Figure modified with permission from Reference 27.

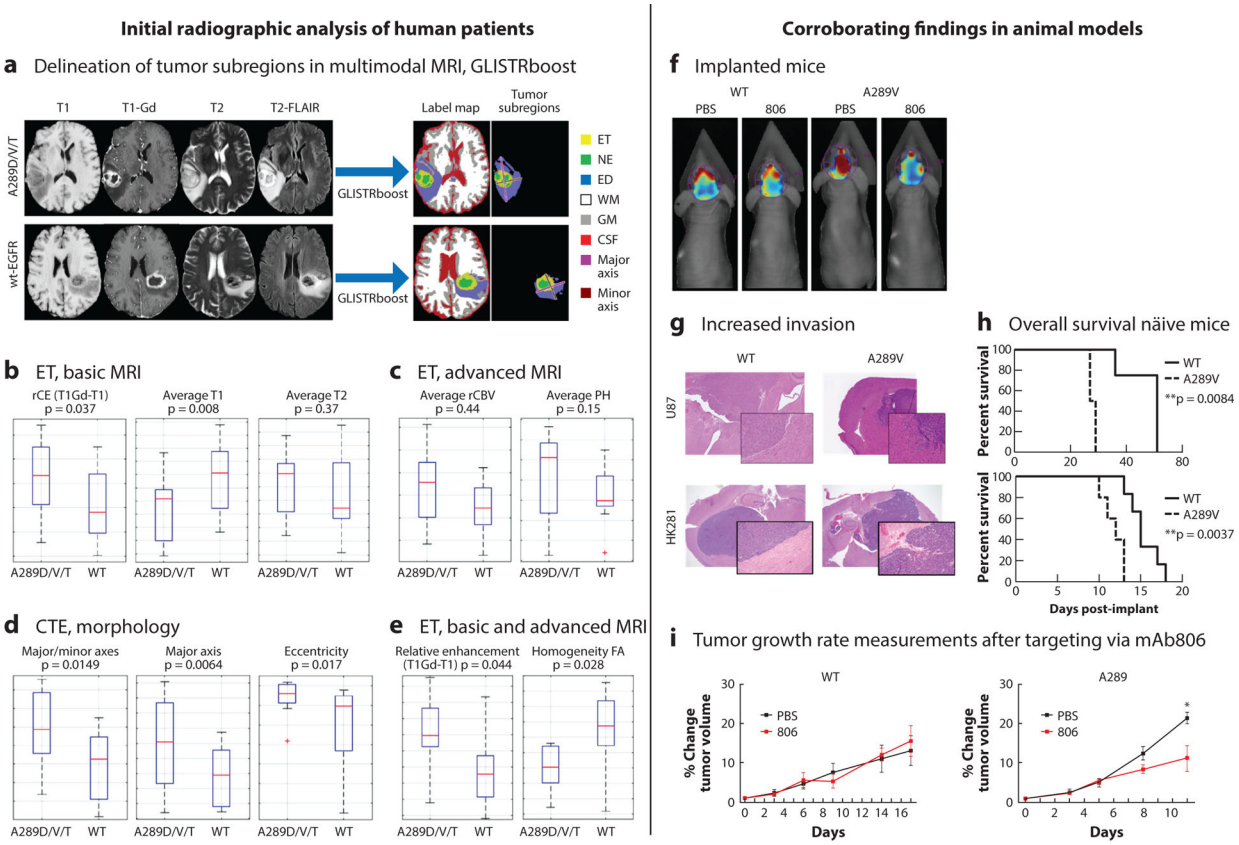


**Figure 6.**

Summary of computational radiographic analysis incorporating biophysical growth modeling (*a*–*e*) (96) leading to the discovery of a potential molecular target, presenting an opportunity for potential therapeutic development (22, 25). The findings of the radiographic analysis were corroborated in mice implanted with tumors (*f*,*h*), the histological analysis of which (*g*) shows increased invasion. (*i*) The implanted tumor growth rate was shown to be much decreased after targeting via mAb806. Abbreviations: CSF, cerebrospinal fluid; CTE, complete tumor extent; ED, edematous/tumor-infiltrated tissue; EGFR, epidermal growth factor receptor; ET, enhancing tumor; GLISTR, Glioma Image Segmentation and Registration; GM, gray matter; MRI, magnetic resonance imaging; NE, necrotic and nonenhancing; PBS, phosphate-buffered saline; PH, peak height of perfusion signal; rCBV, relative cerebral blood volume; rCE, relative contrast enhancement; WM, white matter; WT, whole tumor. Figure modified with permission from Binder ZA, Thorne AH, Bakas S, Wileyto EP, Bilello M, et al. 2018. Epidermal growth factor receptor extracellular domain mutations in glioblastoma present opportunities for clinical imaging and therapeutic development. *Cancer Cell* 34:163–77.

**Table 1**

Clinical problems addressed through integration of mathematical modeling with medical imaging data

| Clinical problem | References |
|---|---|
| Tumor grading and profiling | 67, 69, 70 |
| Molecular characterization | 15, 19–22, 24, 25, 27 |
| Growth prediction | 45–47, 52, 72–78 |
| Infiltration margins (surgical planning) | 79–81 |
| Planning of radiotherapy | 41, 44, 82–84 |
| Prognosis and survival prediction | 48, 59, 67, 68, 85, 86 |
| Tumor recurrence prediction | 61, 64, 66 |
| Prediction and modeling of treatment response | 39, 41, 50, 51, 80, 87–90 |
| Improvement of imaging workflows | 4, 31, 32, 91–99 |